energies

MDPI

Article

Performance Boundaries of Hybrid Photovoltaic–Battery Inverters Under Dynamic, Unbalanced, and Grid Disturbance Conditions

Plamen Stanchev [1,*] and Nikolay Hinov [2]

[1] Department of Intelligent Technology in Industry, Faculty of Computer Systems and Technologies, Technical University of Sofia, 1000 Sofia, Bulgaria
[2] Department of Computer Systems, Faculty of Computer Systems and Technologies, Technical University of Sofia, 1000 Sofia, Bulgaria; hinov@tu-sofia.bg
* Correspondence: p.stanchev@tu-sofia.bg

Abstract

Hybrid photovoltaic (PV)–battery inverters are increasingly required to provide functions extending beyond conventional energy conversion, including zero-export operation, battery coordination, grid support, and backup supply. However, rated power and peak efficiency alone do not adequately describe their practical operating limits. This study proposes a multi-scenario dynamic assessment framework for a 10 kW hybrid PV–battery inverter under twelve normal and stressed operating conditions. The model includes PV curtailment dynamics, a first-order Thevenin battery representation with State of Charge (SOC)-, current-, voltage-, and power-dependent constraints, DC-link energy balance, *dq*-frame current control, current circle limitation, low-voltage ride-through (LVRT)-oriented reactive-current support, and grid-connected/islanded operation. The simulations reveal distinct limitation mechanisms that remain hidden under nominal conditions. Peak unintended export reaches approximately 3.50 kW following sudden load rejection and 3.94 kW at high battery SOC. Nonlinear loading increases the current-related comparative harmonic stress indicator to H_I = 10.73, while a severe grid voltage sag increases it to H_I = 14.30, produces a maximum DC-link deviation of approximately 4.66%, and activates current saturation during 10.83% of the simulation interval. Under islanded overload, peak unserved power reaches approximately 1.45 kW, corresponding to 0.278 Wh of unserved energy. A Hybrid Inverter Stress Index (HISI) is introduced as a secondary normalized measure for cross-scenario comparison, with the highest value of approximately 0.530 obtained during the voltage-sag case. The results demonstrate that hybrid inverter capability should be assessed using dynamic power balance, battery headroom, DC-link, current limitation, comparative harmonic stress, and supply capability indicators in addition to conventional rated specifications.

Keywords: hybrid inverter; photovoltaic system; battery energy storage system; zero-export control; state of charge; DC-link dynamics; current limiting; low-voltage ride-through; nonlinear load; islanded operation; power quality

Check for updates

Academic Editors: Saher Javaid and Iacovos Ioannou

Received: 8 September 2026
Revised: 9 October 2026
Accepted: 13 October 2026
Published: 15 October 2026

Copyright: © 2026 by the authors. Licensee MDPI, Basel, Switzerland. This article is an open access article distributed under the terms and conditions of the Creative Commons Attribution (CC BY) license.

1. Introduction

The accelerating deployment of distributed photovoltaic (PV) generation and battery energy storage systems (BESSs) is fundamentally changing the architecture and operation of low- and medium-voltage electrical networks. At the interface between these distributed

energy resources, local loads, and the utility grid, the power electronic inverter has evolved from a conventional DC–AC conversion stage into a multifunctional energy management device. Modern hybrid PV–battery inverters may simultaneously perform photovoltaic maximum power-point tracking (MPPT), battery charging and discharging, DC-link regulation, active- and reactive-power control, voltage support, export limitation, grid code compliance, and transition between grid-connected and islanded operation [1–4]. Consequently, the performance of the hybrid inverter increasingly determines not only the energy efficiency of the installation but also its dynamic flexibility, power quality, grid interaction, and backup capability.

Recent research has therefore focused extensively on the coordinated operation of PV generation, battery storage, and smart inverter functions [2–8]. Energy management strategies have been developed to improve self-consumption, reduce grid dependence, regulate voltage, coordinate storage operation, and mitigate the variability associated with solar generation [3–7]. At the same time, improvements in power electronic control have expanded the functionality of PV inverters beyond conventional maximum power extraction toward active network support and autonomous energy management [1,8–10]. These developments are particularly important in distribution networks with high penetration of inverter-based resources, where bidirectional power flows and reduced conventional generation increasingly affect the electrical operating environment.

Despite this progress, hybrid inverter performance is still commonly described using a comparatively limited set of manufacturer specifications. Typical parameters include rated active power, maximum apparent power, peak or weighted conversion efficiency, maximum battery charging and discharging power, supported battery voltage range, and selected harmonic or grid code indicators. Such parameters are essential for equipment selection, but they predominantly characterize nominal or steady-state operation. They provide considerably less information about the actual system response when several converter, battery, grid, and load constraints interact dynamically.

This distinction between rated capability and practical dynamic capability is central to the present study. A hybrid inverter can operate with high mean conversion efficiency and remain within its rated active-power boundary while temporarily violating another important operating requirement. Examples include unintended grid export following sudden load rejection, excessive current demand during voltage sag, increased harmonic distortion under nonlinear loads, restricted surplus power absorption at high battery SOC, or the inability to maintain the complete local load after transition to islanded operation. These phenomena have different physical origins and cannot be adequately characterized by a single steady-state performance indicator.

One particularly relevant example is the management of reverse power flow. Increasing penetration of distributed PVs can produce power export from customer installations toward the distribution network, especially during periods of high solar generation and low local consumption. Reverse power flow may contribute to voltage rise problems, increased network control requirements, and restrictions on the permissible amount of distributed generation [11–13]. For this reason, zero-export and export limitation strategies are increasingly used in residential, commercial, and industrial PV installations.

A typical zero-export controller coordinates PV curtailment, battery charging, and utility grid exchange so that surplus locally generated power is prevented from being injected into the upstream grid [11–17]. In a steady state, such strategies can maintain grid power close to the desired export threshold. However, a fundamental dynamic limitation exists: neither photovoltaic curtailment nor battery power can change instantaneously. Following a rapid reduction in load demand, the difference between available generation

and consumption must temporarily be absorbed by the battery, stored in the DC-link capacitor, curtailed at the PV source, or exported to the utility grid.

Therefore, zero-export capability should not necessarily be interpreted as a binary steady-state property. A system capable of maintaining approximately zero export after reaching equilibrium may nevertheless produce a substantial but short-duration reverse power transient. The practical severity of this phenomenon can be described more meaningfully using quantities such as peak unintended export power, exported transient energy, and zero-export violation duration. Existing studies on PV curtailment, battery-assisted export management, and reverse power mitigation demonstrate the importance of coordinating generation and storage [11–18], but transient export excursions associated with the dynamic interaction of these elements deserve additional attention.

Battery state of charge introduces another important operating constraint. Battery storage is frequently considered a flexible resource capable of compensating PV fluctuations and balancing local demand. However, this flexibility is inherently state-dependent. Close to the lower SOC boundary, the available discharge capability is progressively restricted, whereas close to the upper SOC boundary, the ability to absorb surplus generation is reduced. SOC-aware voltage and energy management strategies have consequently been proposed to coordinate storage operation while respecting battery constraints [19–22].

From the perspective of hybrid inverter dynamics, battery headroom can be interpreted as an operational reserve. A battery operating at a moderate SOC may rapidly absorb a temporary PV surplus following load rejection. The same inverter connected to an almost fully charged battery can have significantly less charging reserve, even though the nominal battery capacity remains unchanged. The remaining excess power must then be handled primarily through PV curtailment, the DC link, or the utility grid interface. Thus, high stored energy and high dynamic flexibility are not necessarily equivalent operating objectives.

A second major limitation arises from the finite current capability of the power electronic converter. Unlike synchronous generators, inverter-based resources cannot generally provide large multiples of their rated current during abnormal network conditions. Their maximum current is constrained by semiconductor safe operating limits, thermal stress, magnetic components, and protection requirements. Current limiting is therefore fundamental to inverter protection, but it also directly modifies the converter's dynamic behaviour during network disturbances [23–30].

Recent studies of grid-forming and grid-connected converters have shown that current-limiting strategies can significantly affect transient stability, voltage support, synchronization, fault recovery, and the interaction between the converter and the surrounding power system [23–36]. Different approaches, including current-reference saturation, virtual impedance, power-reference modification, and hybrid limiting methods, offer different compromises between rapid device protection and system-level dynamic performance [23–30]. Consequently, the current limiter should not be regarded as a secondary protection element that becomes relevant only during extreme faults. Once activated, it effectively defines the available inverter control space.

This issue is particularly important during low-voltage ride-through (LVRT). During a grid voltage sag, the converter current required to transfer a given active power increases as the terminal voltage decreases. At the same time, grid support requirements may require additional reactive-current injection to assist voltage recovery. Active- and reactive-current components must therefore share the same finite semiconductor current capability [24–36]. If reactive-current support is prioritized, the available active-current margin decreases. Conversely, maintaining active-power transfer may restrict reactive support. Current circle

limitation consequently represents an inherent physical trade-off rather than a purely algorithmic problem.

Voltage disturbances also affect the DC-side energy balance. If the AC-side converter cannot transfer the power supplied by the PV and battery subsystems because its current capability has been reached, the resulting power imbalance can appear as a DC-link voltage excursion. The severity of this response depends on converter control, DC-link capacitance, battery dynamics, PV curtailment, grid voltage magnitude, and current priority strategy. These interactions make voltage-sag operation especially suitable for exposing practical inverter limitations that are not visible from steady-state rated-power data.

Power quality represents another dimension of the problem. Hybrid inverters increasingly supply loads containing rectifiers, switched-mode power supplies, electronic drives, and other nonlinear devices. Nonlinear and unbalanced loading can increase current distortion and converter stress even when the average active-power balance remains satisfactory. Thus, an inverter may maintain stable DC-link voltage, acceptable root mean square (RMS) current, and high conversion efficiency while simultaneously experiencing significant degradation of current waveform quality. Studies of inverter-dominated and islanded microgrids have highlighted the importance of harmonic performance, load characteristics, and control design under non-ideal operating conditions [31–33,37–39].

Islanded operation further changes the physical role of the hybrid inverter. While connected to the utility grid, temporary deficits in local generation can be compensated by grid import [40,41]. Following disconnection, this external balancing resource is removed, and the inverter must establish or maintain the local electrical supply using only the available PV generation, battery storage, and converter capacity. The practical backup capability is therefore determined by the instantaneous combination of PV power, battery discharge capability, inverter apparent-power rating, reactive load, and maximum current [37–39].

This distinction becomes especially important during islanded overload. A manufacturer may specify a particular nominal or backup power, yet the actual load that can be sustained may be lower when reactive-power demand, SOC constraints, or semiconductor current limits are simultaneously active. Under these conditions, the relevant system-level result is not only inverter efficiency or current magnitude, but also the amount of load that cannot be supplied. Peak unserved power and unserved energy therefore provide useful complementary indicators for evaluating backup performance.

Hardware-in-the-loop and power-hardware-in-the-loop studies are increasingly being used to examine converter behaviour under such dynamic conditions and to bridge the gap between simulation models and practical inverter implementations [39]. Nevertheless, comprehensive experimental testing of every combination of PV variation, SOC condition, grid disturbance, nonlinear loading, and islanded overload can be costly and time-consuming. A computationally efficient multi-scenario modelling framework is therefore useful for initially identifying the operating conditions that deserve more detailed switching-level or experimental investigation.

The existing literature provides substantial knowledge on hybrid PV–battery energy management [1–10], export limitation and reverse power mitigation [11–18], SOC-aware battery coordination [19–22], inverter current limiting and LVRT [23–36], and islanded or power quality operation [37–39]. However, these topics are commonly addressed as separate control or application problems. Consequently, comparatively limited attention has been devoted to evaluating them within a single framework specifically designed to reveal different classes of hidden performance limitations in the same hybrid PV–battery inverter.

A further research gap concerns the comparison of scenarios governed by different physical mechanisms. Efficiency cannot directly quantify a zero-export excursion; total

harmonic distortion (THD) cannot represent loss of load during islanding; and RMS current alone cannot describe DC-link stress or battery absorption limitations. A multi-domain assessment is therefore required if the objective is to characterize the practical operating envelope rather than only one subsystem or one disturbance type.

To address these gaps, this study develops a multi-scenario dynamic assessment framework for a hybrid PV–battery inverter. Twelve operating conditions are investigated, including rated operation, low loading, sudden load increase, load rejection, rapid PV power reduction and recovery, low and high battery SOC, unbalanced loading, nonlinear loading, severe grid voltage sag, and islanded overload. The model incorporates PV curtailment dynamics, SOC-dependent battery constraints, DC-link energy balance, *dq*-frame current control, converter current circle limitation, LVRT-oriented reactive-current support, grid-connected and islanded modes, reduced-order converter losses, and comparative harmonic stress indicators.

Rather than attempting to identify a single universal inverter deficiency, the proposed framework distinguishes several different limitation mechanisms. These include transient zero-export violation, reduced battery absorption reserve, harmonic degradation, current-limited grid support, DC-link stress, and insufficient islanded supply capability. This distinction is important because mitigation of one limitation does not necessarily improve another. For example, increasing battery SOC improves stored energy availability for backup operation but simultaneously reduces charging headroom for transient surplus absorption.

To facilitate comparison between such physically different operating conditions, a composite HISI is introduced. The index combines normalized contributions associated with efficiency degradation, DC-link voltage deviation, harmonic distortion, transient power imbalance, unintended export, current saturation, and unserved energy. The HISI is not intended as an absolute lifetime or reliability indicator; rather, it provides a common comparative scale for identifying which scenarios impose the most significant overall operating stress.

The principal contributions of the present study can be summarized as follows:

1. A unified twelve-scenario assessment framework is developed to investigate hybrid PV–battery inverter performance beyond conventional rated-power and efficiency specifications.
2. Zero-export operation is evaluated dynamically using peak unintended export power, transient exported energy, and export violation duration, allowing short-duration reverse power events to be distinguished from steady-state export control.
3. Battery SOC is explicitly incorporated as a dynamic flexibility constraint, enabling the influence of reduced charging headroom near the upper SOC limit and reduced discharge capability near the lower SOC limit to be assessed.
4. A *dq*-based inverter model with current circle limitation and LVRT-oriented reactive-current support is employed to investigate the interaction between active-power transfer, reactive support, DC-link dynamics, and finite semiconductor current capability.
5. Nonlinear and unbalanced loading are included to distinguish power quality limitations from purely energy- or current-based performance degradation.
6. Islanded overload capability is evaluated using current saturation, peak unserved power, and unserved energy, thereby distinguishing practical backup capability from nominal inverter power.
7. The Hybrid Inverter Stress Index is proposed to provide a unified comparative measure across operating scenarios governed by fundamentally different physical limitations.

The proposed framework is intended as a generic assessment methodology rather than a performance model of a specific commercial product. Its purpose is to identify operating

boundaries that may remain hidden when hybrid inverters are characterized primarily by nominal power and peak efficiency. The results presented in the following sections demonstrate that the practical performance envelope is governed by the interaction of converter current capability, battery state constraints, control bandwidth, power quality, grid conditions, and local load requirements.

The remainder of this paper is organized as follows. Section 2 describes the hybrid PV–battery architecture, dynamic models, control structure, investigated scenarios, performance indicators, and HISI formulation. Section 3 presents the simulation results and cross-scenario comparison. Section 4 discusses the broader implications and limitations of the proposed methodology, while Section 5 summarizes the principal conclusions and future research directions.

2. Materials and Methods

2.1. System Architecture and Modelling Framework

The investigated system represents a grid-connected hybrid PV–battery inverter with optional islanded operation. The architecture consists of a photovoltaic source, a battery energy storage system, a common DC link, a bidirectional power conversion stage, a three-phase inverter, and a utility grid/load interface. The battery is connected to the DC link through a bidirectional DC/DC converter, while the PV source is represented as a controllable DC power source with curtailment capability.

The general architecture of the investigated hybrid PV–battery inverter system is illustrated in Figure 1. The figure presents the main power conversion stages and the associated control structure, including the PV curtailment logic, battery power control, DC-link regulation, *dq* current control, and the grid/load interface.

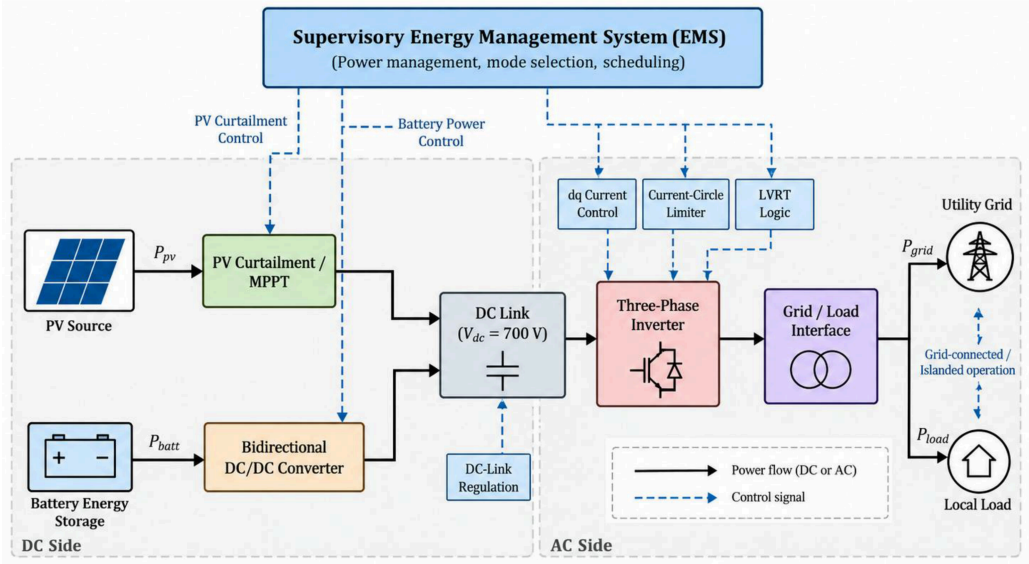


Figure 1. The general architecture of the investigated hybrid PV–battery inverter system, including the photovoltaic source, bidirectional battery interface, common DC link, three-phase inverter, supervisory control, and grid/load connection.

The model was developed in Python 3.10 using an averaged dynamic representation. This approach was selected to enable efficient simulation of multiple operating scenarios while retaining the main dynamic interactions among the PV source, battery, DC link, inverter current limits, grid interface, and supervisory energy management system.

The overall power balance is governed by the interaction among photovoltaic generation, battery power, grid exchange, local load demand, and converter losses. Positive

battery power denotes battery discharge toward the DC link, while negative battery power denotes charging. Positive grid power denotes import from the utility grid, whereas negative grid power denotes unintended export.

The principal system parameters used in the simulations are summarized in Table 1.

Table 1. Main parameters of simulated hybrid PV–battery inverter system.

Parameter	Symbol	Value
Rated inverter active power	P_{rated}	10 kW
Rated inverter apparent power	S_{rated}	10 kVA
Rated PV power	$P_{\text{PV,rated}}$	12 kW
Grid line-to-line RMS voltage	V_{LL}	400 V
Nominal DC-link voltage	$V_{\text{DC,ref}}$	700 V
DC-link capacitance	C_{DC}	30 mF
PV control time constant	τ_{PV}	0.12 s
Current control time constant	τ_{i}	0.004 s
Maximum inverter current	I_{max}	1.2 pu
LVRT threshold	V_{LVRT}	0.90 pu
Simulation time step	Δt	0.5 ms
Total simulation time	t_{sim}	6 s

The inverter current limit was defined as 1.2 pu relative to the rated RMS current. For a 10 kVA, 400 V three-phase converter, this corresponds to a rated RMS current of approximately 14.43 A and a maximum RMS current of approximately 17.32 A.

The complete simulation framework constitutes a coupled reduced-order differential–algebraic model. Dynamic states are represented by ordinary differential equations for the PV power response, battery polarization and state of charge, DC-link voltage, and inverter *dq* currents. Algebraic relationships are used for instantaneous active- and reactive-power calculation, converter current limiting, grid power exchange, apparent-power constraints, unserved-load calculation, and performance indicator evaluation.

The individual physical relations employed in the model are based on established power electronic and energy storage modelling principles and are not claimed as newly derived component models. In particular, the synchronous reference-frame power equations, DC-link energy balance, first-order converter dynamics, current circle limitation, and Thevenin battery representation follow conventional reduced-order modelling approaches. The original contribution of the present work lies in their integration within a common multi-scenario assessment framework, the explicit evaluation of transient export, SOC-dependent operating headroom, current-limited grid support, and islanded supply deficiency, and the proposed HISI-based cross-scenario aggregation.

The model is therefore intended as a system-level screening and specification support tool, rather than as a detailed electromagnetic-transient or manufacturer-specific digital twin. Its objective is to identify which subsystem or control constraint becomes dominant under different operating conditions before more computationally intensive switching-level, hardware-in-the-loop, or experimental validation is undertaken.

2.2. Photovoltaic Source Model

The photovoltaic subsystem is represented by an available power input $P_{\text{PV,av}}(t)$ and a first-order curtailed power response. The available power represents the maximum DC power that can be extracted from the PV array under the prescribed irradiance condition. Detailed cell-level and switching converter dynamics are not included because the objective of the model is the system-level transient interaction between PV generation, battery storage, the DC link, and the grid-side inverter.

The actual PV power is governed by

$$\tau_{PV}\frac{dP_{PV}}{dt} = P_{PV,ref} - P_{PV}, \quad (1)$$

where P_{PV} is the actual photovoltaic power, $P_{PV,ref}$ is the curtailed power reference, and τ_{PV} is the effective PV control time constant. In the simulations, τ_{PV} = 0.12 s.

Under normal conditions,

$$P_{PV,ref} = P_{PV,av}, \quad (2)$$

whereas during a local power surplus, the supervisory controller reduces the PV power reference according to

$$P_{PV,ref} = sat[P_{PV,av} - P_{sur} - K_{PV,V}\max(V_{DC} - V_{DC,ref},0)], \quad (3)$$

with

$$P_{sur} = \max(P_{PV,av} + P_{batt} - P_{load},0). \quad (4)$$

The saturation operator constrains the resulting PV reference between zero and the instantaneous available PV power. This representation reproduces the finite response of the curtailment mechanism and is therefore able to generate short-duration surplus power transients after abrupt changes in local demand.

The PV control dynamics are intentionally slower than the battery power control dynamics. This separation of time constants represents the supervisory nature of PV curtailment and is important for investigating temporary zero-export violations. The model is not intended to reproduce semiconductor switching dynamics or detailed MPPT perturbation behaviour.

2.3. Battery Energy Storage Model

The battery energy storage system is represented using a first-order Thevenin equivalent-circuit model (ECM), selected as a compromise between physical interpretability and computational efficiency. In contrast to the initial energy-only representation, the revised model explicitly includes the open-circuit voltage dependence on state of charge, ohmic voltage drop, polarization dynamics, terminal voltage constraints, and charge/discharge current limits. This refinement enables the short-term electrical response of the battery to influence the transient power-sharing behaviour of the hybrid inverter.

A lithium iron phosphate (LFP) battery chemistry is assumed. The simulated storage system has a nominal energy capacity of 15 kWh and a nominal pack voltage of approximately 400 V. The first-order Thevenin model consists of an SOC-dependent open-circuit voltage source V_{OC}, a series ohmic resistance R_0, and one polarization branch represented by R_1 and C_1.

The battery terminal voltage is calculated as

$$V_b = V_{OC}(SOC) - R_0 I_{batt} - V_p, \quad (5)$$

where I_{batt} is positive during discharge and negative during charging, and V_p is the polarization voltage.

The polarization dynamics are described by

$$\frac{dV_p}{dt} = -\frac{V_p}{R_1 C_1} + \frac{I_{batt}}{C_1}. \quad (6)$$

The instantaneous battery power is then obtained from

$$P_{\text{batt}} = V_{\text{batt}} I_{\text{batt}}. \tag{7}$$

Positive P_{batt} denotes discharge toward the common DC link, whereas negative P_{batt} denotes battery charging.

The battery state of charge is updated using Coulomb counting:

$$\frac{dSOC}{dt} = -\frac{\eta_c I_{\text{batt}}}{3600 Q_{\text{pack}}} \tag{8}$$

where Q_{pack} is the equivalent pack capacity in ampere-hours and η_c is selected according to the charging or discharging direction. The nominal equivalent pack capacity is calculated from

$$Q_{\text{pack}} = \frac{E_{\text{batt}}}{V_{\text{pack,nom}}}, \tag{9}$$

which gives Q_{pack} = 37.5 Ah for the adopted 15 kWh, 400 V system.

The electrical parameters of the first-order ECM are obtained from reference-cell parameters and scaled to the equivalent pack level. The reference LFP cell has a nominal voltage of 3.3 V and a nominal capacity of 2.3 Ah. The adopted cell-level first-order parameters are $R_{0,\text{cell}}$ = 13.04 mΩ, $R_{1,\text{cell}}$ = 1.90 mΩ, and $C_{1,\text{cell}}$ = 41.61 F.

Equivalent series and parallel scaling factors are defined as

$$N_s^{\text{eq}} = \frac{V_{\text{pack,nom}}}{V_{\text{cell,nom}}} \tag{10}$$

and

$$N_p^{\text{eq}} = \frac{Q_{\text{pack}}}{Q_{\text{cell}}}. \tag{11}$$

The corresponding pack-equivalent parameters are calculated as

$$R_{0,\text{pack}} = R_{0,\text{cell}} \frac{N_s^{\text{eq}}}{N_p^{\text{eq}}}, \tag{12}$$

$$R_{1,\text{pack}} = R_{1,\text{cell}} \frac{N_s^{\text{eq}}}{N_p^{\text{eq}}} \tag{13}$$

and

$$C_{1,\text{pack}} = C_{1,\text{cell}} \frac{N_s^{\text{eq}}}{N_p^{\text{eq}}}. \tag{14}$$

The equivalent scaling is used only to obtain physically consistent pack-level electrical dynamics for the generic 15 kWh storage system. It is not intended to represent a specific integer series/parallel module topology of a commercial battery product.

The LFP open-circuit voltage is represented using a piecewise-linear SOC-dependent characteristic. This approximation reproduces the characteristic relatively flat mid-SOC voltage plateau and the steeper voltage variation near the low- and high-SOC regions.

The cell-level open-circuit voltage is defined using interpolation between representative SOC and voltage points and subsequently scaled to the pack level:

$$V_{\text{OC,pack}} = N_s^{\text{eq}} V_{OC,cell}(SOC) \tag{15}$$

The operational SOC range is restricted to $0.20 \leq \text{SOC} \leq 0.90$.

Unlike the previous model version, no arbitrary linear power derating is imposed within a fixed SOC margin. Instead, charging and discharging capability is determined by the interaction between SOC limits, battery current limits, terminal voltage boundaries, and maximum battery power.

The battery power reference generated by the supervisory EMS is converted into a current request by solving

$$P_{\text{batt,ref}} = (V_{\text{OC}} - V_p - R_0 I_{\text{batt}}) I_{\text{batt}}. \tag{16}$$

This leads to the quadratic relationship

$$R_0 I_{\text{batt}}^2 - \left(V_{\text{OC}} - V_p\right) I_{\text{batt}} + P_{\text{batt,ref}} = 0. \tag{17}$$

The physically relevant solution close to P/V is used as the requested battery current. The current is subsequently constrained by

$$-I_{\text{ch,max}} \leq I_{\text{batt}} \leq I_{\text{dis,max}}, \tag{18}$$

together with the battery power limits of 6 kW during charging and 7 kW during discharge.

The terminal voltage constraints are

$$V_{\text{batt,min}} \leq V_{\text{batt}} \leq V_{\text{batt,max}}. \tag{19}$$

For the adopted LFP representation, the cell-level operational voltage range is 3.00–3.45 V and is scaled to the equivalent pack voltage using N_s^{eq}.

When the SOC reaches the minimum boundary, further discharge is inhibited. Similarly, when the SOC reaches the maximum boundary, further charging is prevented. Thus, the available battery flexibility emerges from explicit electro-electrical constraints rather than from an imposed SOC-dependent derating function.

This behaviour is particularly relevant to scenarios S7 and S8. In S7, operation near the lower SOC boundary restricts the ability of the battery to provide additional discharge power. In S8, operation near the upper SOC boundary reduces the available charging capability and therefore limits the ability of the storage system to absorb a sudden PV surplus.

The adopted first-order Thevenin representation is intended to capture the dominant battery dynamics over the second-scale horizon of the present study. Higher-order electrochemical diffusion effects, detailed thermal coupling, cell-to-cell imbalance, ageing, capacity fade, and long-term state-of-health evolution are outside the scope of the present model.

To ensure consistency between the revised battery model and its numerical implementation, the principal parameters of the LFP battery equivalent-circuit representation are summarized in Table 2. In addition to the system-level energy, voltage, SOC, and power limits, the table includes the reference-cell parameters used to derive the pack-equivalent first-order Thevenin model.

Table 2. Main parameters of revised LFP battery energy storage model and first-order Thevenin equivalent circuit.

Parameter	Symbol	Value
Battery chemistry	—	LFP
Nominal battery energy	E_{batt}	15 kWh
Nominal pack voltage	$V_{pack,nom}$	400 V
Equivalent pack capacity	Q_{pack}	37.5 Ah
Minimum SOC	SOC_{min}	20%
Maximum SOC	SOC_{max}	90%
Maximum discharge power	$P_{batt,dis,max}$	7 kW
Maximum charging power	$P_{batt,ch,max}$	6 kW
Discharge efficiency	$\eta_{batt,dis}$	95.5%
Charging efficiency	$\eta_{batt,ch}$	95.5%
Reference-cell nominal voltage	$V_{cell,nom}$	3.3 V
Reference-cell capacity	Q_{cell}	2.3 Ah
Cell ohmic resistance	$R_{0,cell}$	13.04 mΩ
Cell polarization resistance	$R_{1,cell}$	1.90 mΩ
Cell polarization capacitance	$C_{1,cell}$	41.61 F
Equivalent series scaling factor	N_s^{eq}	121.21
Equivalent parallel scaling factor	N_p^{eq}	16.30
Pack-equivalent ohmic resistance	$R_{0,pack}$	0.09694 Ω
Pack-equivalent polarization resistance	$R_{1,pack}$	0.01413 Ω
Pack-equivalent polarization capacitance	$C_{1,pack}$	5.597 F
Minimum pack voltage	$V_{batt,min}$	363.64 V
Maximum pack voltage	$V_{batt,max}$	418.18 V
Maximum discharge current	$I_{batt,dis,max}$	17.5 A
Maximum charging current	$I_{batt,ch,max}$	15.0 A

2.4. DC-Link Dynamic Model

The common DC link is represented by a lumped capacitor with capacitance C_{DC}. The DC-link stored energy is

$$E_{DC} = \frac{1}{2} C_{DC} V_{DC}^2. \tag{20}$$

The corresponding dynamic energy balance is expressed as

$$C_{DC} V_{DC} \frac{dV_{DC}}{dt} = P_{PV} + P_{batt} - P_{inv} - P_{loss}, \tag{21}$$

where P_{PV} and P_{batt} are the DC-side source powers, P_{inv} is the active power transferred by the inverter to the AC side, and P_{loss} represents converter losses.

Accordingly, the DC-link voltage dynamics are calculated as

$$\frac{dV_{DC}}{dt} = \frac{P_{PV} + P_{batt} - P_{inv} - P_{loss}}{C_{DC} V_{DC}}. \tag{22}$$

The nominal DC-link voltage is 700 V and the DC-link capacitance is 30 mF. Thus, any temporary mismatch between DC-side generation and AC-side power transfer appears as a DC-link voltage excursion.

A proportional DC-link correction term is included in the battery power reference:

$$P_{batt,ref} = P_{load} - P_{PV,av} + K_V (V_{DC,ref} - V_{DC}) \tag{23}$$

This feedback assists the energy management layer in restoring the DC-link voltage following rapid power disturbances.

2.5. Three-Phase Inverter and dq Current Model

The three-phase inverter is represented in a synchronous *dq* reference frame aligned with the positive-sequence grid voltage. Under this orientation, the q-axis grid voltage component is assumed to be approximately zero.

The instantaneous active and reactive powers are therefore expressed as

$$P = \frac{3}{2} V_d I_d \tag{24}$$

and

$$Q = -\frac{3}{2} V_d I_d. \tag{25}$$

The corresponding current references are as follows:

$$I_{d,\mathrm{ref}} = \frac{P_{\mathrm{inv,ref}}}{1.5 V_d} \tag{26}$$

$$I_{q,\mathrm{ref}} = -\frac{Q_{\mathrm{inv,ref}}}{1.5 V_d} \tag{27}$$

The inner current control dynamics are approximated using first-order responses:

$$\tau_i \frac{dI_d}{dt} = I_{d,\mathrm{lim}} - I_d \tag{28}$$

$$\tau_i \frac{dI_q}{dt} = I_{q,\mathrm{lim}} - I_q \tag{29}$$

where $I_{d,\mathrm{lim}}$ and $I_{q,\mathrm{lim}}$ are the current references after application of the converter current constraint, and τ_i is the effective current control time constant specified in Table 1.

The RMS phase-current magnitude is obtained from

$$I_{\mathrm{RMS}} = \frac{\sqrt{I_d^2 + I_q^2}}{\sqrt{2}}. \tag{30}$$

For the investigated 10 kVA, 400 V three-phase inverter,

$$I_{\mathrm{rated}} = \frac{S_{\mathrm{rated}}}{\sqrt{3} V_{LL}} \approx 14.43\mathrm{A}. \tag{31}$$

Under normal grid conditions, if the requested current exceeds this boundary, the *d*- and *q*-axis current references are proportionally scaled while preserving their ratio. During voltage-sag operation, a different priority rule is applied, as described in Section 2.6, where reactive-current support is given priority over active-current transfer.

This averaged formulation captures the principal interaction between active-power transfer, reactive-power support, and finite inverter current capability while avoiding the computational cost of explicit pulse-width modulation (PWM) switching simulation.

2.6. Grid Voltage Sag, LVRT, and Current Limitation

During normal grid-connected operation, the grid voltage magnitude is assumed to remain close to its nominal value. In the voltage-sag scenario, the grid voltage is intentionally reduced below the predefined LVRT threshold in order to activate the inverter support logic.

The sag severity is defined as

$$\Delta V_{\mathrm{sag}} = \max(V_{\mathrm{LVRT}} - V_{\mathrm{g}}, 0), \tag{32}$$

where V_g is the instantaneous grid voltage magnitude per unit and V_{LVRT} is the activation threshold specified in Table 1.

When $\Delta V_{sag} > 0$, the inverter generates an additional reactive-current support reference according to

$$I_{q,sup} = K_q \Delta V_{sag} I_{rated}, \tag{33}$$

where K_q is the reactive-current support gain and I_{rated} is the rated inverter RMS current.

The corresponding reactive-power support command is obtained from

$$Q_{sup} = \sqrt{3} V_{LL} I_{q,sup}, \tag{34}$$

subject to the apparent-power and current capability of the inverter.

During LVRT operation, reactive current is assigned priority. The q-axis current reference is therefore first constrained by the maximum converter current:

$$I_{q,lim} = sat(I_{q,ref}, -I_{max,dq}, I_{max,dq}) \tag{35}$$

The remaining active-current capability is then calculated from the current circle constraint as

$$|I_{d,max}| = \sqrt{I_{max,dq}^2 - I_{q,max}^2}. \tag{36}$$

The active-current reference is subsequently limited to

$$-I_{d,max} \leq I_{d,lim} \leq I_{d,max}. \tag{37}$$

This control structure reproduces the physical competition between active-power transfer and reactive-current support during severe voltage reduction. As reactive-current demand increases, the available active-current margin decreases, even if the commanded active power remains unchanged.

The adopted LVRT representation is intentionally generic. It is designed to evaluate the interaction between voltage support, current limitation, DC-link dynamics, and power transfer rather than to reproduce the proprietary fault-response logic of a specific commercial inverter.

2.7. Supervisory Energy Management System

The Supervisory Energy Management System (EMS) coordinates the PV source, battery storage, DC-link regulation, grid exchange, and inverter operating mode. The EMS operates at each simulation time step using the measured or calculated system states P_{load}, $P_{PV,av}$, SOC, V_{DC}, grid voltage, and grid connection status.

The principal objective in grid-connected mode is to supply the local load while minimizing unintended export and maintaining the DC-link voltage close to its reference value.

The initial residual-power demand is defined as

$$P_{res} = P_{load} - P_{PV,av}. \tag{38}$$

The preliminary battery power reference is

$$P_{batt,ref}^{*} = P_{res} + K_V (V_{DC,ref} - V_{DC}). \tag{39}$$

The battery command is then constrained according to battery state and electrical limits:

$$P_{batt,ref} = \mathrm{sat}\left(P_{batt,ref}^{*}, P_{batt,min}, P_{batt,max}\right) \tag{40}$$

After determining the achievable battery power, any remaining local surplus is calculated as

$$P_{\text{sur}} = \max(P_{\text{PV,av}} + P_{\text{batt}} - P_{\text{load}}, 0). \tag{41}$$

This surplus activates PV curtailment. Because the battery and PV control loops have finite and different response times, the power balance is not restored instantaneously, allowing transient reverse power events to occur naturally within the model.

The EMS also monitors the grid voltage. When the LVRT condition is detected, reactive-current support is activated and the current circle limiter modifies the available active-current reference.

The complete EMS decision sequence is as follows:

1. Acquire the system states;
2. Determine grid-connected or islanded mode;
3. Calculate residual active-power demand;
4. Calculate battery power reference;
5. Apply battery SOC, current, voltage, and power constraints;
6. Calculate remaining surplus or deficit;
7. Update PV curtailment reference;
8. Determine active and reactive inverter references;
9. Apply LVRT logic where required;
10. Enforce the inverter current circle constraint;
11. Update converter and DC-link states;
12. Calculate grid exchange or unserved load;
13. Record the performance indicators.

2.8. Grid-Connected and Islanded Mode Transition

The reactive-power reference is determined separately according to the operating mode. Under normal grid-connected conditions, no additional reactive support is imposed by the supervisory layer. During a voltage sag, the LVRT strategy described in Section 2.6 generates the required reactive-current support. In islanded operation, the inverter additionally supplies the local reactive load demand.

The EMS therefore provides coordination between the slower PV curtailment response, the electrically constrained battery model, DC-link regulation, and the inverter current control layer. The detailed battery, DC-link, *dq*-current, and LVRT equations are given in Sections 2.3–2.6 and are not repeated here.

$$P_{\text{grid}} = P_{\text{load}} - P_{\text{inv}} \tag{42}$$

Positive P_{grid} denotes utility import and negative P_{grid} denotes export.

When the grid connection state changes from connected to disconnected, the grid power exchange is constrained to $P_{\text{grid}} = 0$, $Q_{\text{grid}} = 0$.

The local inverter must then supply both active and reactive load demand from the available PV and battery resources.

The maximum available active power in islanded mode is limited simultaneously by the DC-side power availability and the apparent-power/current capability of the inverter:

$$P_{\text{inv}} = \min[P_{\text{load}}, P_{\text{DC,av}}, P_{I,\max}] \tag{43}$$

where:

$$P_{\text{DC,av}} = P_{\text{PV}} + \max(P_{\text{batt}}, 0) \tag{44}$$

and

$$P_{\mathrm{I,max}} = \sqrt{S_{\mathrm{max}}^2 - Q_{load}^2} \tag{45}$$

If the demanded load exceeds the available inverter output,

$$P_{\mathrm{unserved}} = \max(P_{\mathrm{load}} - P_{\mathrm{inv}}, 0). \tag{46}$$

The corresponding unserved energy is calculated as

$$E_{\mathrm{unserved}} = \int P_{\mathrm{unserved}} dt. \tag{47}$$

This formulation allows the islanded operating capability to be evaluated independently from the utility grid and makes it possible to distinguish between limitations caused by insufficient DC-side power availability and those caused by the inverter apparent-power/current boundary.

2.9. Converter Loss and Efficiency Model

The inverter losses are represented using a reduced-order empirical formulation intended for comparative scenario assessment rather than device-level semiconductor loss prediction. The instantaneous converter losses are expressed as

$$P_{\mathrm{loss}} = P_0 + k_1 I_{\mathrm{RMS}} + k_2 I_{\mathrm{RMS}}^2, \tag{48}$$

where P_0 represents approximately load-independent auxiliary and control losses, k_1 represents the current-proportional component, and k_2 represents the quadratic current-dependent component.

The instantaneous conversion efficiency is calculated as

$$\eta_{\mathrm{inv}} = \frac{|P_{\mathrm{inv}}|}{|P_{\mathrm{inv}}| + P_{\mathrm{loss}}}. \tag{49}$$

The calculated converter losses are included consistently in both the supervisory power balance calculation and the DC-link energy balance. Thus, changes in inverter loading affect not only the reported conversion efficiency but also the power available for battery coordination and DC-link regulation.

For scenario-level comparison, the mean inverter efficiency is evaluated only during intervals in which the absolute inverter active power exceeds 200 W. This threshold avoids assigning disproportionate weight to numerical efficiency values at near-zero power transfer.

The adopted loss model is intended for comparative system-level assessment and does not reproduce semiconductor-specific switching losses, dead-time effects, junction temperature dependence, gate-drive behaviour, or detailed conduction characteristics. These effects would require a switching-level device model and are outside the scope of the present study.

2.10. Comparative Harmonic Stress Indicator

Because the present inverter representation is based on an averaged dq model, it does not explicitly reproduce switching harmonics, dead-time effects, carrier-frequency components, or the complete phase-current waveform required for formal total harmonic distortion (THD) calculation. Therefore, the quantities used in this study are interpreted as comparative harmonic stress indicators rather than as standard-compliant THD predictions.

Two dimensionless indicators are introduced: a current-related harmonic stress indicator H_{I} and a voltage-related harmonic stress indicator H_{V}. Their purpose is to provide a consistent relative measure of the additional electrical stress associated with nonlinear loading, load unbalance, current saturation, voltage sag, and very low-load operation.

The current-related indicator is defined as

$$H_I = H_{I,0} + K_{\mathrm{nl}}\lambda_{\mathrm{nl}} + K_{\mathrm{ub}}\lambda_{\mathrm{ub}} + K_{\mathrm{sat}}S_I + K_V\Delta V_{\mathrm{sag}} + K_{\mathrm{L}}\lambda_{\mathrm{low}}, \tag{50}$$

where $H_{\mathrm{I},0}$ is the baseline value, λ_{nl} represents the nonlinear load severity, λ_{ub} represents the load unbalance severity, S_{I} denotes activation of the inverter current limit, ΔV_{sag} represents voltage-sag severity, and λ_{low} accounts for the increased relative distortion sensitivity at very low loading.

Similarly, the voltage-related indicator is expressed as

$$H_V = H_{V,0} + K_{\mathrm{nl}}\lambda_{\mathrm{nl}} + K_{\mathrm{ub}}\lambda_{\mathrm{ub}} + K_{\mathrm{sat}}S_V + K_V\Delta V_{\mathrm{sag}}. \tag{51}$$

The nonlinear load and unbalance coefficients are activated only in the corresponding scenarios, whereas the saturation and voltage-sag terms respond dynamically to the electrical state of the inverter.

These indicators are used only for relative cross-scenario comparison and for the harmonic stress contribution to the composite assessment index. They should not be interpreted as measured or simulated THD values, nor as evidence of compliance with harmonic limits specified by grid standards.

This distinction is important because the averaged model is intended to investigate system-level interactions among power balance, battery limitations, current saturation, grid disturbances, and islanded operation rather than detailed switching-frequency power quality.

2.11. Simulation Sequence and Flowchart

To provide a clear overview of the interaction among the individual subsystem models and the supervisory control logic, the complete simulation sequence is summarized in Figure 2. The computational procedure follows a fixed-step sequential update in which the operating scenario defines the external conditions, while the supervisory EMS coordinates the PV source, battery subsystem, DC link, inverter, and grid interface.

At the beginning of each simulation, the scenario-specific initial conditions and operating profiles are loaded, including the initial battery SOC, load demand, available PV power, grid voltage condition, and grid connection state. The principal dynamic states are then initialized, including the DC-link voltage, battery polarization voltage, battery SOC, actual PV power, and dq inverter currents.

At each simulation step, the following sequence is applied:

1. The current load demand, available PV power, grid voltage magnitude, and grid connection state are obtained from the active scenario profile.
2. The supervisory EMS evaluates the residual active-power demand and determines the preliminary battery power reference, including the DC-link voltage correction.
3. The battery power command is processed by the first-order Thevenin model. The requested current is calculated and constrained by the applicable SOC, current, terminal voltage, and charge/discharge power limits.
4. The achievable battery power is used together with the available PV power to determine whether PV curtailment is required. The PV power reference is then updated according to the finite first-order PV response.

5. The inverter active-power reference is calculated from the resulting DC-side power after accounting for the converter loss estimate.
6. The operating mode is evaluated. Under grid-connected conditions, the grid compensates for the remaining local power imbalance. Under islanded conditions, the supplied load is limited by the available DC-side power and inverter apparent-power/current capability.
7. When the grid voltage falls below the LVRT threshold, the reactive-current support logic is activated. The q-axis current demand is assigned priority, and the remaining *d*-axis current capability is determined from the current circle constraint.
8. The resulting *dq* current references are applied to the first-order current control dynamics, and the inverter RMS current is calculated.
9. Converter losses are evaluated from the updated inverter current and are included in the power balance calculation.
10. The battery polarization state, battery SOC, PV power state, inverter current states, and DC-link voltage are advanced to the next numerical time step.
11. Grid exchange, unserved power, current saturation state, and the comparative harmonic stress indicators are recorded.
12. After completion of the simulation interval, the scenario-level performance indicators are calculated from the stored time-series data and used for the cross-scenario comparison and composite stress assessment.

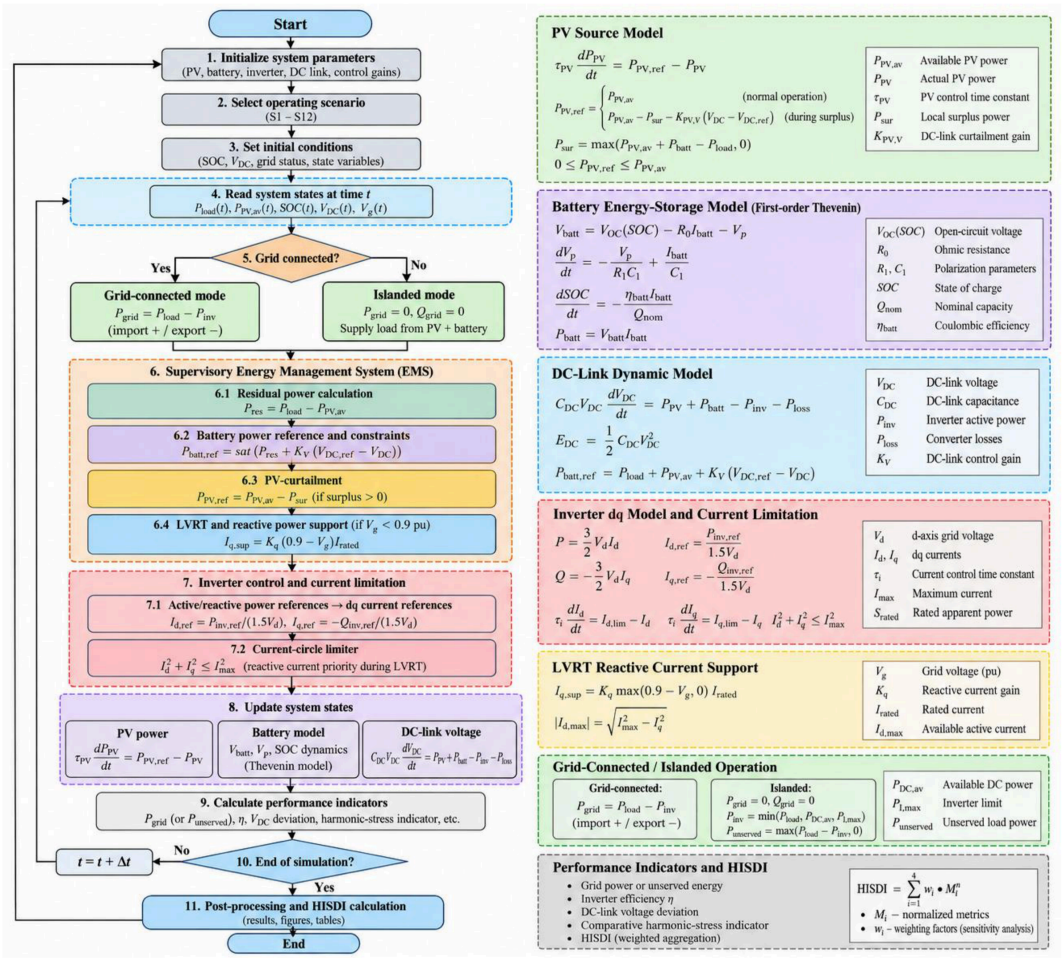


Figure 2. The simulation and supervisory Energy Management System (EMS) flowchart with the principal mathematical models of the hybrid PV–battery inverter, including PV curtailment, battery dynamics, DC-link energy balance, dq current control, LVRT support, current limitation, grid-connected/islanded operation, and performance assessment.

The complete sequence is illustrated in Figure 2.

2.12. Investigated Operating Scenarios

The hybrid PV–battery inverter was evaluated under twelve operating scenarios selected to represent both normal operating conditions and distinct dynamic or constraint-dominated stress cases. The scenarios were designed to isolate different limitations associated with conversion efficiency, transient power balance, battery operating boundaries, load characteristics, grid disturbances, and islanded supply capability.

The investigated cases are summarized in Table 3.

Table 3. Investigated operating scenarios and the corresponding primary performance limitation.

Scenario	Operating Condition	Primary Phenomenon Investigated
S1	Rated operation	Reference performance
S2	Low-load operation	Partial-load efficiency
S3	Sudden load increase	Dynamic power deficit
S4	Sudden load rejection	Transient zero-export limitation
S5	Rapid PV power drop	Battery response to generation loss
S6	Rapid PV recovery	Power redistribution after PV recovery
S7	Low battery SOC	Reduced discharge capability
S8	High battery SOC	Reduced charging headroom
S9	Unbalanced load	Unbalance-related electrical stress
S10	Nonlinear load	Comparative harmonic stress
S11	Grid voltage sag	LVRT and current circle limitation
S12	Islanded overload	Backup capability and unserved load

Scenario S1 is used as the reference condition for comparison with the remaining cases. S2 evaluates the effect of reduced converter loading on efficiency, whereas S3 and S4 investigate the transient response to abrupt increases and decreases in local demand.

Scenarios S5 and S6 represent rapid changes in photovoltaic generation and are used to evaluate short-term redistribution of power among the PV source, battery, inverter, and utility interface.

Scenarios S7 and S8 examine operation close to the lower and upper battery SOC boundaries, respectively. In S7, the available battery discharge capability becomes constrained near the minimum permitted SOC. In S8, the limited charging headroom restricts the ability of the battery to absorb a sudden local power surplus.

Scenarios S9 and S10 address load-related electrical stress. S9 introduces load unbalance, whereas S10 introduces nonlinear load severity and is assessed using the comparative harmonic stress indicators defined in Section 2.10. These indicators are used for relative comparison and are not interpreted as switching-level THD measurements.

Scenario S11 introduces a severe grid voltage sag. The grid voltage is reduced to 0.55 pu, thereby activating the LVRT strategy and forcing simultaneous allocation of the finite inverter current capability between active-power transfer and reactive-current support. The current manuscript already defines this case as a grid voltage sag, not as a detailed short-circuit fault simulation.

Finally, S12 represents islanded overload operation. Following grid disconnection, the local load is temporarily increased to 12.5 kW, causing the hybrid inverter to operate close to its combined DC-side power and AC-side current capability. The resulting unserved power and unserved energy are used to quantify the backup limitation.

2.13. Performance Indicators

The performance of each operating scenario is quantified using a common set of electrical, dynamic, power balance, storage, and supply capability indicators. The purpose of this multi-indicator assessment is to identify operating limitations that may remain hidden if the hybrid inverter is evaluated only from rated power and mean conversion efficiency.

The principal performance indicators are as follows:

- The mean inverter efficiency;
- The peak unintended grid export;
- Zero-export violation duration;
- Transient exported energy;
- The maximum DC-link voltage;
- The minimum DC-link voltage;
- The maximum absolute DC-link voltage deviation;
- The peak instantaneous power imbalance;
- The accumulated absolute energy imbalance;
- The maximum current-related harmonic stress indicator H_I;
- The maximum voltage-related harmonic stress indicator H_V;
- Current saturation duration;
- The peak RMS inverter current;
- The peak unserved power;
- Unserved energy;
- Final battery SOC.

The peak unintended grid export is defined as

$$P_{\mathrm{exp,pk}} = \max[-P_{\mathrm{grid}}(t), 0]. \tag{52}$$

The exported transient energy is calculated as

$$E_{\mathrm{exp}} = \int \max\left[-P_{\mathrm{grid}}(t), 0\right] dt. \tag{53}$$

The export violation duration is defined as the accumulated interval during which the reverse grid power exceeds the numerical detection threshold used for post-processing.

The maximum relative DC-link deviation is calculated from

$$\Delta V_{\mathrm{DC,max}} = \max_t \left| \frac{V_{\mathrm{DC}}(t) - V_{\mathrm{DC,ref}}}{V_{\mathrm{DC,ref}}} \right| \cdot 100\%. \tag{54}$$

The maximum values of H_I and H_V are used only as comparative harmonic stress quantities, consistent with Section 2.10, and are not interpreted as standard-compliant THD values.

Together, these indicators provide a common quantitative basis for comparing scenarios governed by different limiting mechanisms, including transient export, battery constraints, DC-link excursions, current saturation, harmonic-related stress, and loss of load in islanded operation.

2.14. Hybrid Inverter Stress Index

To facilitate cross-scenario comparison, a composite Hybrid Inverter Stress Index (HISI) is introduced. The index combines several normalized indicators associated with distinct electrical and operational limitations of the hybrid inverter.

The HISI is defined as

$$\mathrm{HISI} = \sum_{j=1}^{N} \omega_j D_j, \tag{55}$$

subject to

$$\sum_{j=1}^{7} \omega_j = 1, \qquad \omega_j \geq 0, \tag{56}$$

where D_j represents a normalized performance degradation component and ω_j is the corresponding weighting coefficient.

The seven normalized components are associated with the following:

- Conversion efficiency penalty;
- The maximum DC-link voltage deviation;
- Comparative harmonic stress;
- The transient power imbalance;
- Unintended grid export;
- Inverter current saturation;
- Unserved energy.

For the present implementation, the normalized components are calculated as follows:

$$D_\eta = \mathrm{clip}\left(\frac{97.5 - \eta}{12}, 0, 1\right) \tag{57}$$

$$D_V = \mathrm{clip}\left(\frac{\Delta V_{\mathrm{DC,max}}}{8}, 0, 1\right) \tag{58}$$

$$D_H = \mathrm{clip}\left(\frac{H_I}{15}, 0, 1\right) \tag{59}$$

$$D_P = \mathrm{clip}\left(\frac{P_{\mathrm{imb,pk}}}{3500}, 0, 1\right) \tag{60}$$

$$D_{\mathrm{exp}} = \mathrm{clip}\left(\frac{P_{\mathrm{exp,pk}}}{4000}, 0, 1\right) \tag{61}$$

$$D_I = \mathrm{clip}\left(\frac{T_{\mathrm{sat}}}{20}, 0, 1\right) \tag{62}$$

$$D_U = \mathrm{clip}\left(\frac{E_{\mathrm{unserved}}}{2}, 0, 1\right) \tag{63}$$

Here, clip(x,0,1) restricts each normalized contribution to the interval [0,1]. The normalization constants are used as reference scaling quantities to place indicators with different physical units on a common dimensionless basis. They do not represent mandatory regulatory limits.

The weighting coefficients adopted for the baseline comparison are

$$\boldsymbol{\omega} = [0.10, 0.14, 0.14, 0.16, 0.14, 0.16, 0.16]. \tag{64}$$

Slightly greater weights are assigned to transient power imbalance, current saturation, and unserved energy because these quantities directly reflect a loss of operating margin or the inability to satisfy the requested converter function. Nevertheless, the weighting scheme is not treated as unique or universally optimal.

To examine the dependence of the composite index on the selected weights, a sensitivity analysis is performed by independently perturbing the baseline weights by up to $\pm 30\%$ and subsequently renormalizing them so that their sum remains equal to unity. The

individual physical indicators reported in Section 2.13 remain unchanged by this procedure; only their aggregation into the HISI is affected.

Accordingly, the HISI is used as a secondary comparative indicator rather than as the sole basis for interpreting scenario severity. The individual electrical and operational metrics remain the primary quantities used to identify the physical limitation associated with each operating condition.

2.15. Numerical Procedure, Simulation Horizon, and Data Processing

All simulations are implemented in Python 3.10 using a fixed numerical time step of $\Delta t = 0.5$ ms. Each operating scenario is simulated independently over a total interval of 6 s using the same system model and parameter set, with only the scenario-specific operating profiles and initial conditions modified.

The selected simulation horizon is intended to capture fast electrical and supervisory control dynamics associated with load steps, PV power variations, battery power redistribution, DC-link excursions, inverter current limitation, LVRT activation, transient reverse power flow, and transition to islanded operation. It is therefore not intended to represent long-duration energy management behaviour.

At each time step, the subsystem states and algebraic quantities are updated sequentially according to the procedure described in Section 2.11. The dynamic states include the actual PV power, battery polarization voltage, battery SOC, DC-link voltage, and *dq* inverter currents. Algebraic variables include battery terminal voltage and power, grid exchange, converter losses, current limit status, unserved power, and the comparative harmonic stress indicators.

The same numerical time step and solver structure are applied to all twelve scenarios to preserve consistency in the cross-scenario comparison. Scenario-specific disturbances are introduced only through the prescribed load, PV, SOC, grid voltage, and grid-connection profiles.

During each simulation, the principal time-series variables are recorded, including the following:

- PV available and actual power;
- Battery power, current, terminal voltage, SOC, and polarization state;
- Inverter active and reactive power;
- Grid active and reactive power;
- Load demand;
- DC-link voltage;
- *d*- and *q*-axis inverter currents;
- RMS inverter current;
- Converter losses;
- Current saturation state;
- Comparative harmonic stress indicators;
- Unserved power.

Following completion of each simulation, the time-series data are post-processed automatically to obtain the scenario-level indicators defined in Section 2.13. The resulting datasets are exported in comma-separated value (CSV) format, while the numerical summary is used for the cross-scenario analysis presented in Section 3.

The 6 s simulation interval should be interpreted strictly as a short-term dynamic assessment window. It does not capture multi-hour or daily SOC evolution, battery ageing, capacity fade, thermal accumulation, seasonal PV variability, long-term load profiles, or energy management optimization over extended horizons. Similarly, the results are not

used to infer compliance with grid code quantities that require averaging or observation over substantially longer time intervals.

Accordingly, the present framework is intended as a dynamic pre-design and specification support tool for identifying short-term operating boundaries of hybrid PV–battery inverters. Long-duration energy management studies and experimental or hardware-in-the-loop validation remain complementary extensions of the present methodology.

3. Results

The revised hybrid PV–battery inverter model was evaluated under the twelve operating scenarios defined in Section 2.12. The analysis was designed to identify short-term operating limitations that are not evident from rated active power or mean conversion efficiency alone. The investigated cases cover steady-state reference operation, rapid load and PV variations, battery operation close to its SOC boundaries, unbalanced and nonlinear loading, a severe grid voltage sag, and islanded overload.

The assessment is based on the electrical and operational indicators defined in Section 2.13, including mean conversion efficiency, unintended grid export, DC-link voltage deviation, transient power imbalance, comparative harmonic stress, current saturation, RMS inverter current, and unserved load. The Hybrid Inverter Stress Index (HISI) is used only as a secondary aggregate indicator, while the interpretation of each scenario is based primarily on the corresponding physical quantities.

The revised simulations show that different disturbances activate fundamentally different system constraints. Load rejection and high-SOC operation primarily expose limitations in transient surplus power absorption; the nonlinear load case produces elevated comparative harmonic stress without current saturation; the grid voltage sag activates the inverter current boundary and produces the largest DC-link excursion; and islanded overload reveals the finite local supply capability through current saturation and unserved energy. The following subsections examine these limiting mechanisms in detail.

3.1. Reference Rated Operating Condition

Scenario S1 represents the reference operating condition used for comparison with the remaining disturbance and constraint-dominated cases. The inverter supplies a load of approximately 9 kW while the PV subsystem provides approximately 8.5 kW, with the remaining active-power demand coordinated through the battery and grid interfaces.

Under this operating condition, the inverter remains well within its electrical limits. The peak RMS current is approximately 12.99 A, below the imposed maximum RMS current of 17.32 A, and the current-limiting mechanism is not activated. The mean conversion efficiency is approximately 98.50%.

The revised initialization and power balance formulation result in a nearly stationary DC-link condition. The DC-link voltage remains essentially at its 700 V reference value throughout the scenario, with a negligible maximum relative deviation. The peak instantaneous internal power imbalance is only approximately 0.23 W, confirming that the initial operating point is numerically consistent with the corresponding steady-state power balance.

No unintended grid export or unserved load is observed. The comparative harmonic stress indicators remain at their baseline values, with H_I = 1.80 and H_V = 0.90. These quantities are used only as relative stress indicators and should not be interpreted as THD values.

The battery remains within its normal operating region, with the final SOC remaining close to 60%. The resulting HISI value is approximately 0.017, providing a low-stress reference against which the remaining scenarios can be compared.

This reference case therefore confirms that the revised model reproduces stable operation under nominal conditions without activating battery, DC-link, current, export, or supply capability constraints.

3.2. Sudden Load Rejection and Transient Zero-Export Limitation

Scenario S4 was designed to evaluate the transient zero-export capability of the hybrid inverter following an abrupt reduction in local demand. Before the disturbance, the system operates with relatively high PV generation and moderate local consumption. At $t = 2$ s, the load is rapidly reduced, producing an immediate local active-power surplus.

The resulting power-sharing response is presented in Figure 3.

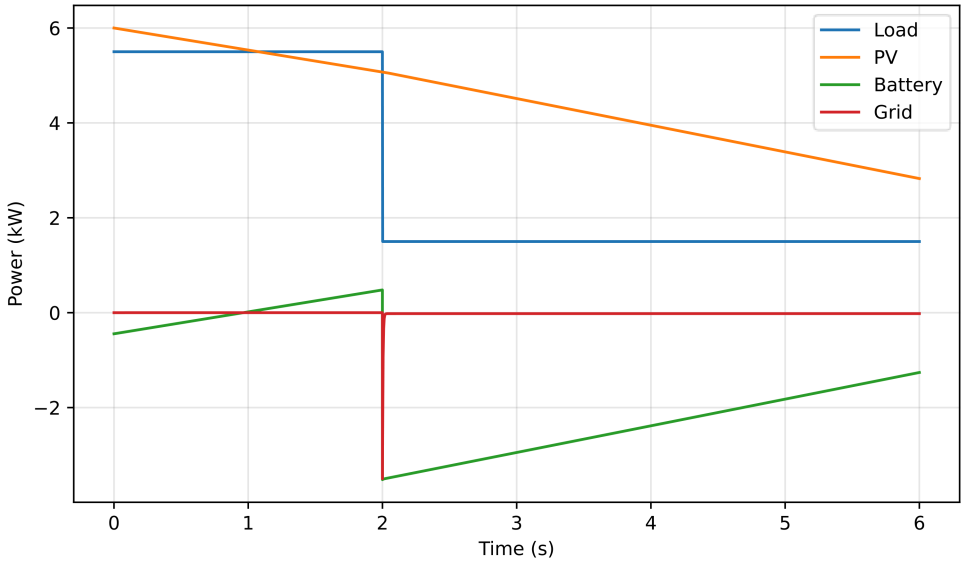


Figure 3. The dynamic power-sharing response during the sudden load rejection scenario (S4), showing the abrupt reduction in load demand and the resulting transient redistribution of the PV, battery, and grid power.

Immediately after load rejection, the battery charging command and PV curtailment controller begin to absorb and reduce the surplus power. However, because these control actions have finite response times, the surplus cannot be redistributed instantaneously. The maximum unintended grid export reaches approximately 3.50 kW, while the associated exported transient energy is approximately 0.026 Wh.

The DC-link voltage response is shown in Figure 4.

The DC-link voltage remains tightly regulated around its nominal value. The maximum absolute relative deviation is approximately 0.095%, demonstrating that the DC-link capacitor and supervisory control successfully buffer the short-duration power imbalance without a significant voltage excursion.

The corresponding RMS inverter current is shown in Figure 5.

The peak RMS inverter current is approximately 7.94 A, remaining well below the imposed maximum current limit. No current saturation occurs during the disturbance. Therefore, the dominant limitation in this scenario is not semiconductor current capability, but the finite bandwidth of the surplus power redistribution process.

The peak instantaneous internal power imbalance reaches approximately 3.50 kW, consistent with the abrupt reduction in load demand. The comparative current-related harmonic stress indicator remains low, with $H_I \approx 2.10$, confirming that harmonic-related stress is not the dominant mechanism in this case.

The resulting HISI value is approximately 0.304, which is substantially higher than in the rated reference condition but remains below the value obtained during severe grid voltage sag.

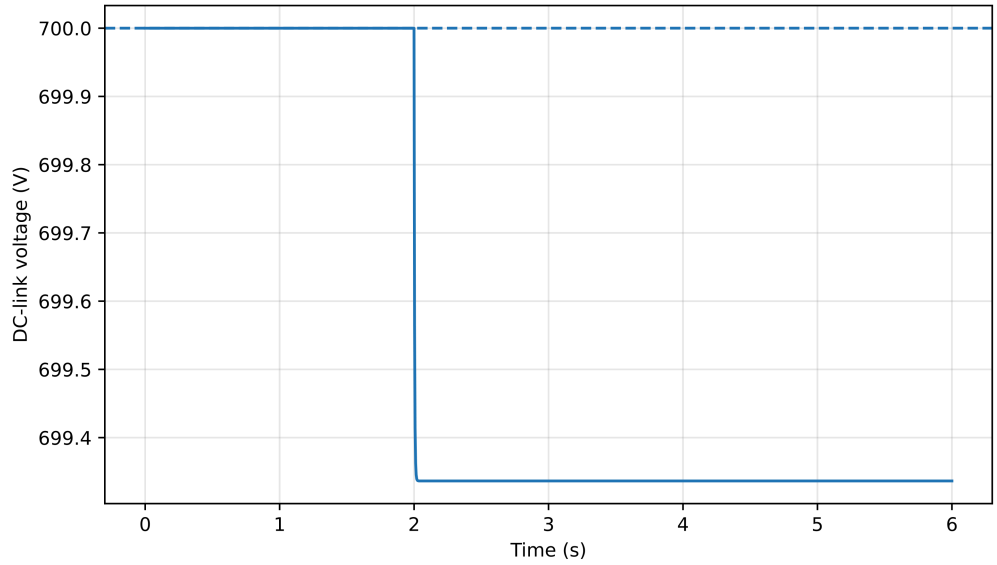


Figure 4. DC-link voltage response during the sudden load rejection scenario (S4). The dashed blue line represents the reference DC-link voltage (700 V), while the solid blue line shows the actual DC-link voltage response.

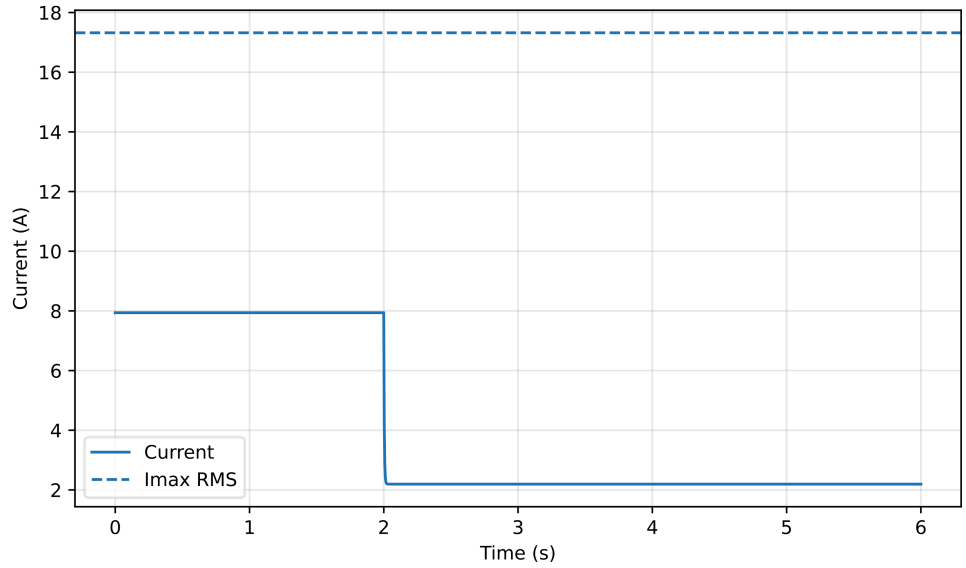


Figure 5. RMS inverter current during sudden load rejection scenario (S4).

3.3. High-SOC Battery Limitation and Increased Export Risk

Scenario S8 investigates the influence of operation close to the upper battery SOC boundary on the ability of the hybrid inverter to absorb a sudden local power surplus. In the revised model, the battery operates close to its maximum permitted SOC while the PV subsystem continues to provide substantial generation. Following the reduction in local demand, the available battery charging headroom becomes limited and a larger fraction of the transient surplus must be handled through PV curtailment and the utility grid interface.

The resulting power-sharing response is presented in Figure 6.

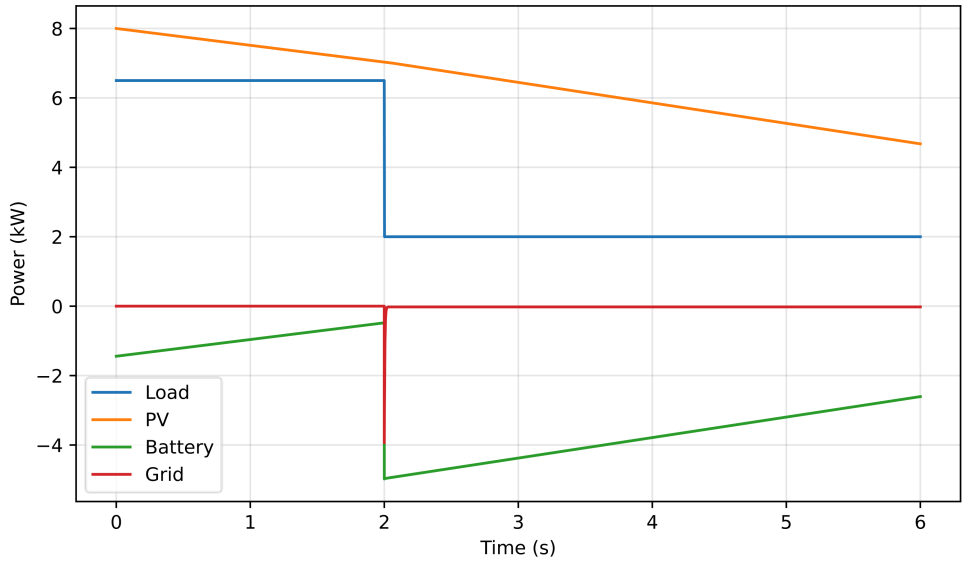


Figure 6. Dynamic power-sharing response under the high-SOC operating condition (S8), illustrating the transient redistribution of the PV, battery, load, and grid power when battery charging headroom is limited.

The maximum unintended grid export reaches approximately 3.94 kW. Although the associated exported energy is only approximately 0.029 Wh, the peak reverse power excursion is larger than that obtained in the sudden load rejection scenario (S4). This comparison demonstrates that transient zero-export performance depends not only on the magnitude of the load change but also on the instantaneous energy absorption capability of the battery.

The corresponding DC-link response is shown in Figure 7.

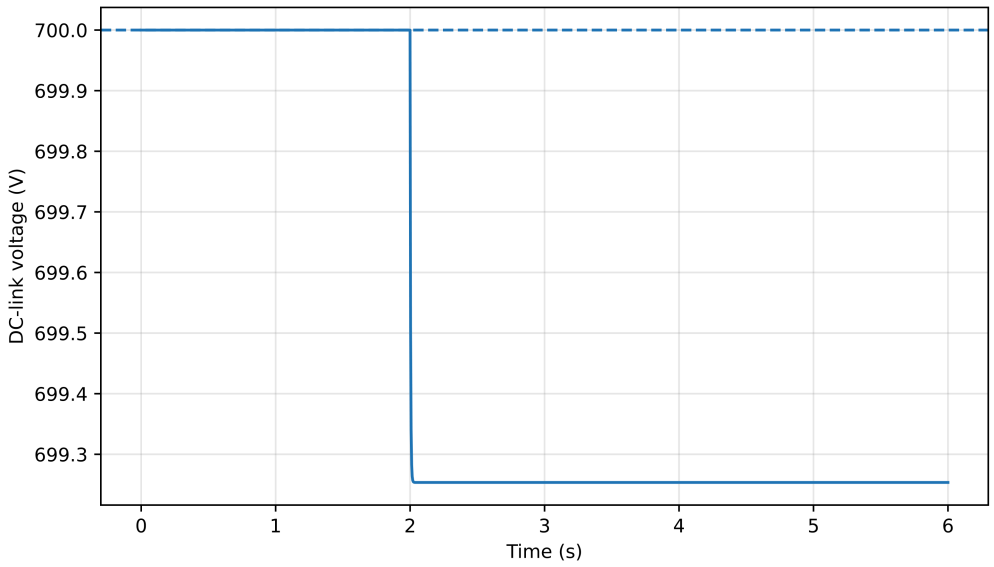


Figure 7. DC-link voltage response during the high-SOC operating scenario (S8). The dashed blue line represents the reference DC-link voltage (700 V), while the solid blue line shows the actual DC-link voltage response.

Despite the restricted charging headroom, the DC link remains well regulated. The maximum absolute relative voltage deviation is approximately 0.107%, indicating that the disturbance does not lead to significant DC-link instability. The peak instantaneous internal

power imbalance reaches approximately 3.94 kW, reflecting the short-duration mismatch created during the redistribution of surplus generation.

The inverter RMS current response is presented in Figure 8.

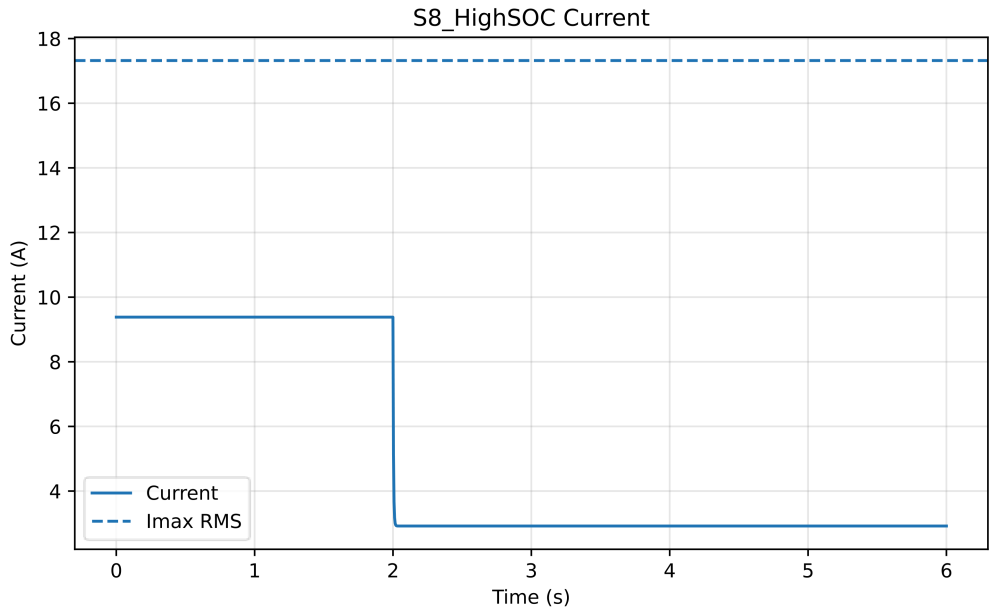


Figure 8. RMS inverter current during high-SOC operating scenario (S8).

The peak RMS inverter current is approximately 9.38 A, remaining substantially below the imposed 17.32 A current limit. No current saturation occurs. Consequently, the dominant restriction in this scenario is associated with battery energy absorption capability rather than the semiconductor current capability of the inverter.

The battery response also confirms that the storage subsystem remains within its electrical boundaries. The final SOC is approximately 89.98%, the maximum terminal voltage is approximately 407.36 V, and the peak battery current magnitude is approximately 12.23 A. These values remain within the limits defined by the revised first-order Thevenin model.

The comparative harmonic stress indicators remain at their baseline levels, with H_I = 1.80 and H_V = 0.90, showing that waveform-related stress is not the principal limitation in this case.

The resulting HISI value is approximately 0.316, slightly higher than the value obtained for S4. The comparison between the two scenarios therefore shows that operation close to the upper SOC boundary can reduce the dynamic flexibility available for suppressing transient reverse power flow, even when the inverter remains far from its current limit and the DC-link voltage remains well controlled.

3.4. Nonlinear Load and Comparative Harmonic Stress

Scenario S10 evaluates the behaviour of the hybrid inverter under nonlinear loading. In contrast to the preceding load rejection and high-SOC scenarios, the principal limitation in this case is not associated with transient active-power redistribution or battery operating headroom. Instead, the scenario aims to examine the increase in the comparative harmonic-related electrical stress represented by the indicators H_I and H_V.

The active-power response is presented in Figure 9.

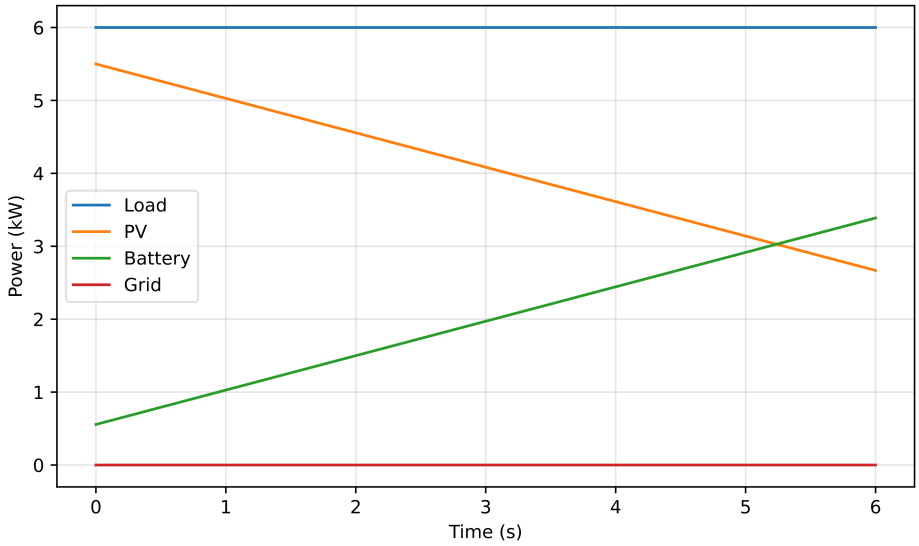


Figure 9. Power-sharing response under the nonlinear load operating scenario (S10), showing the PV, battery, load, and grid active-power trajectories.

The active-power balance remains stable throughout the investigated interval, and no significant unintended export or unserved load is produced. The mean inverter efficiency remains approximately 98.50%, indicating that the nonlinear load condition does not substantially affect the reduced-order conversion efficiency metric.

The corresponding DC-link voltage response is shown in Figure 10.

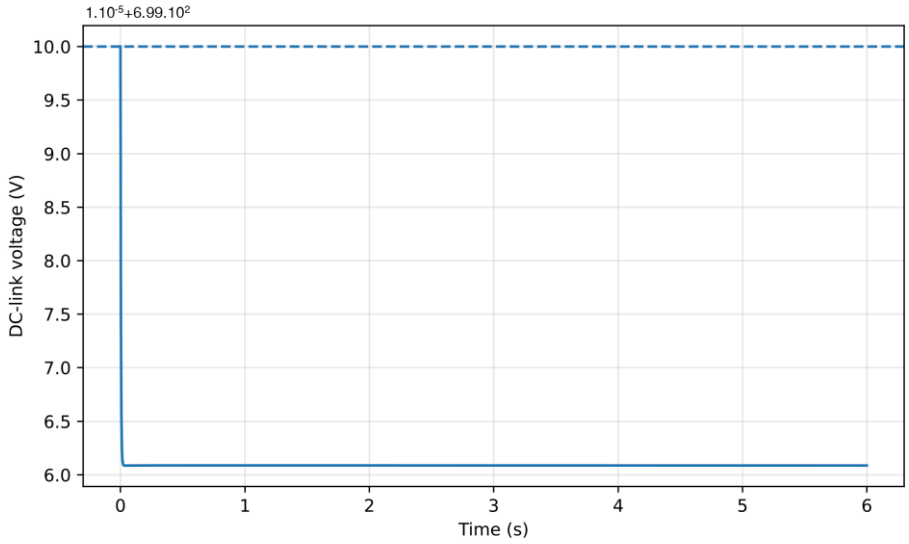


Figure 10. DC-link voltage response during the nonlinear load operating scenario (S10). The dashed blue line represents the reference DC-link voltage (700 V), while the solid blue line shows the actual DC-link voltage response.

The DC-link voltage remains close to its reference value, confirming that the nonlinear load disturbance does not primarily manifest as a DC-side energy balance instability. Thus, conventional quantities such as active-power balance, mean efficiency, and DC-link regulation alone would not identify the principal stress mechanism associated with this scenario.

The RMS inverter current is presented in Figure 11.

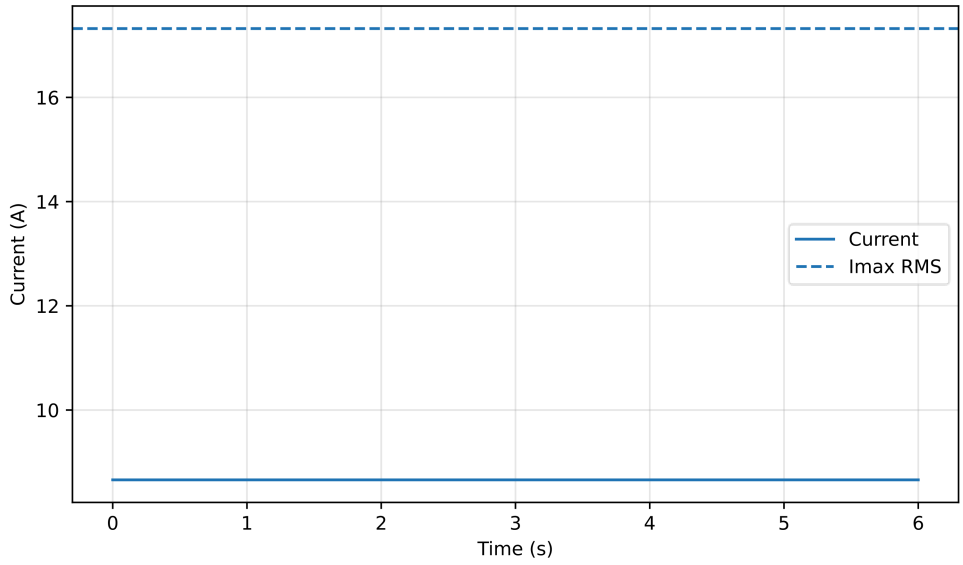


Figure 11. RMS inverter current during the nonlinear load operating scenario (S10).

The inverter remains below the imposed current boundary and the current-limiting mechanism is not activated. Consequently, the nonlinear load scenario does not represent a current capability limitation.

The most pronounced effect appears in the comparative harmonic stress indicators. The maximum current-related indicator increases to $H_I \approx 10.73$, while the maximum voltage-related indicator reaches $H_V \approx 2.69$.

These values are substantially higher than the corresponding baseline values obtained in the rated operating condition, $H_I = 1.80$ and $H_V = 0.90$. However, because the model does not explicitly reproduce switching-frequency waveforms, these quantities are dimensionless comparative stress indicators and not THD percentages.

The resulting HISI value is approximately 0.100, which is higher than the rated reference value but substantially lower than the values associated with transient export, severe voltage sag, or islanded overload. This illustrates an important feature of the proposed multi-domain assessment: a scenario can exhibit comparatively elevated waveform-related stress while remaining well within the inverter's active-power, DC-link, and RMS current operating boundaries.

Therefore, S10 demonstrates that satisfactory active-power balance and conversion efficiency do not necessarily imply low electrical waveform stress. The comparative harmonic indicators provide an additional screening dimension that is not captured by conventional power and current magnitude metrics.

3.5. Grid Voltage Sag, LVRT Response, and Current Saturation

Scenario S11 evaluates the response of the hybrid PV–battery inverter to severe grid voltage sag. During the disturbance interval, the grid voltage is reduced to 0.55 pu, which is well below the LVRT activation threshold defined in Section 2.6. As a result, the controller increases the reactive-current demand while simultaneously attempting to maintain active-power transfer.

The resulting active-power response is presented in Figure 12.

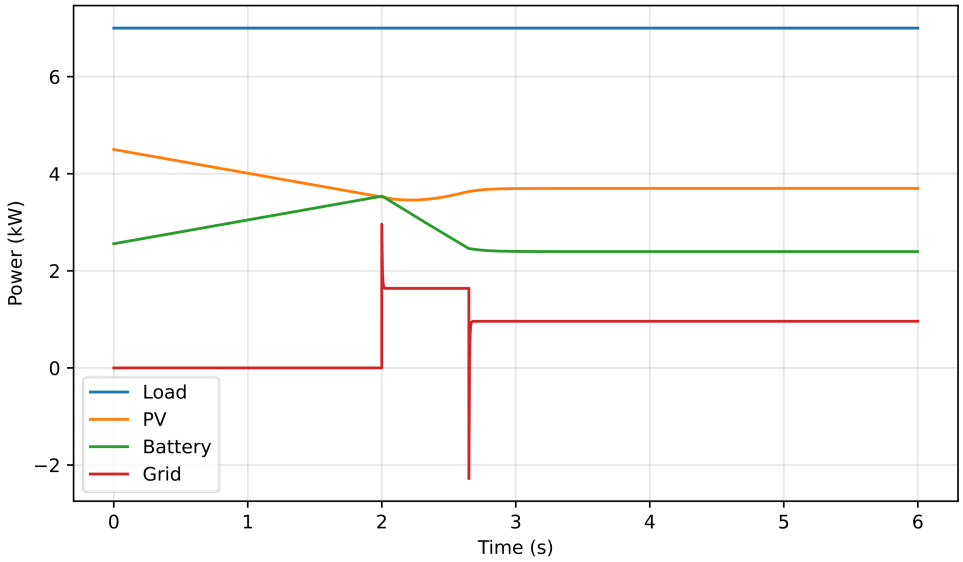


Figure 12. The dynamic power-sharing response during the severe grid voltage sag scenario (S11), showing the redistribution of the PV, battery, inverter, load, and grid active power during LVRT operation.

The voltage reduction increases the current required to transfer a given amount of active power. At the same time, LVRT control introduces additional reactive-current demand. Because both current components must remain inside the finite inverter current circle, the available active-current margin is progressively reduced as reactive support increases.

The corresponding DC-link voltage response is shown in Figure 13.

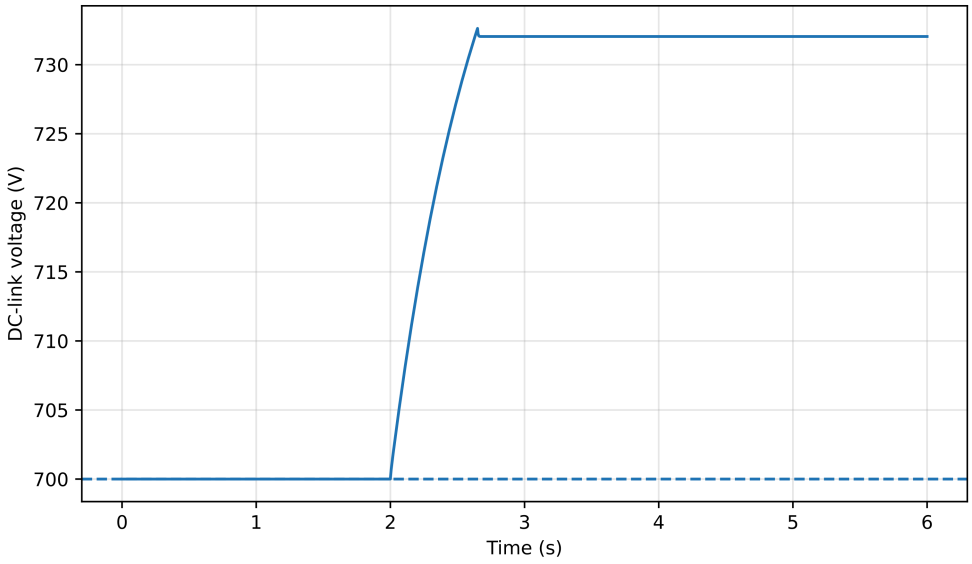


Figure 13. DC-link voltage response during the severe grid voltage sag scenario (S11). The dashed blue line represents the reference DC-link voltage (700 V), while the solid blue line shows the actual DC-link voltage response.

The grid disturbance produces the largest DC-link excursion among the investigated scenarios. The maximum absolute relative DC-link deviation reaches approximately 4.66%. This response reflects the temporary mismatch between the DC-side power supplied by the PV and battery subsystems and the reduced AC-side power transfer capability caused by the inverter current constraint.

The inverter RMS current response is presented in Figure 14.

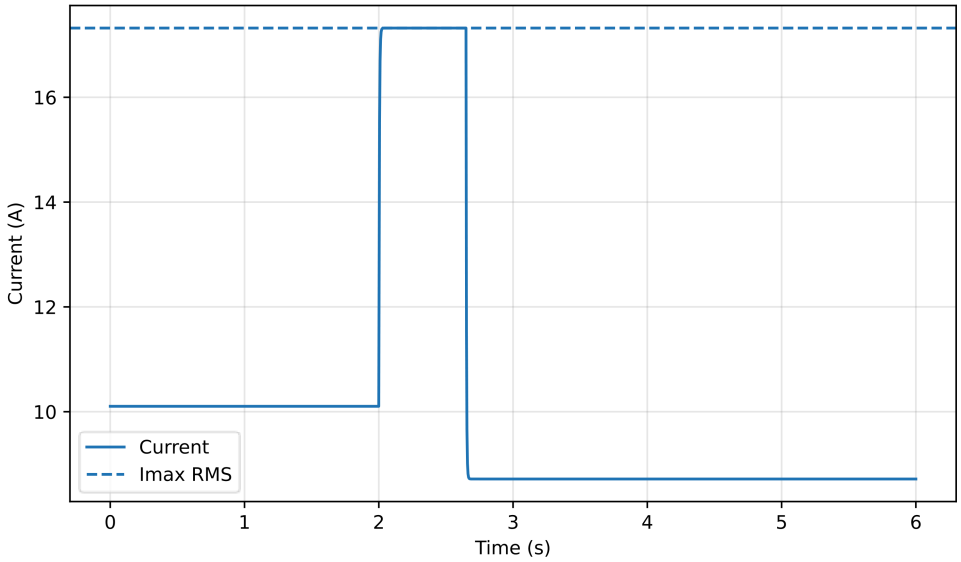


Figure 14. RMS inverter current during the grid voltage sag scenario (S11), showing activation of the imposed current boundary.

The peak RMS inverter current reaches approximately 17.32 A, corresponding to the imposed maximum inverter current. The current-limiting mechanism remains active for approximately 10.83% of the total simulation interval. This confirms that the dominant physical limitation during the sag is the finite current capability of the converter rather than insufficient battery energy or PV availability.

The peak instantaneous power imbalance reaches approximately 3.26 kW, demonstrating the strong coupling between the AC-side voltage disturbance and the DC-side energy balance. A short-duration unintended export excursion is also observed, with a peak value of approximately 2.28 kW; however, this is secondary to the current-limiting and DC-link effects.

The comparative harmonic stress indicators also increase significantly during the disturbance. The maximum values are approximately $H_I \approx 14.30$ and $H_V \approx 5.80$.

These are the highest harmonic-related stress values among the investigated scenarios. As defined in Section 2.10, they should be interpreted only as dimensionless comparative indicators associated with the combined effects of voltage sag and current saturation, rather than as standard-compliant THD values.

The resulting HISI value is approximately 0.530, the highest value obtained among the twelve investigated operating conditions. This high composite value arises because several stress mechanisms occur simultaneously: current saturation, reactive-current prioritization, DC-link deviation, power imbalance, and elevated comparative harmonic stress.

Scenario S11 therefore demonstrates the importance of evaluating voltage-sag operation as a coupled multi-domain constraint problem. The inverter remains operational, but the available control space becomes restricted by the current circle boundary, creating a direct trade-off between active-power transfer and reactive-current support.

3.6. Islanded Overload and Unserved Load

Scenario S12 evaluates the short-term supply capability of the hybrid PV–battery system after transition to islanded operation. Following disconnection from the utility grid, the local load is temporarily increased to approximately 12.5 kW. Because grid support is no longer available, the inverter must supply the load entirely from the instantaneous PV generation, battery discharge capability, and its finite apparent-power and current limits.

The resulting active-power response is presented in Figure 15.

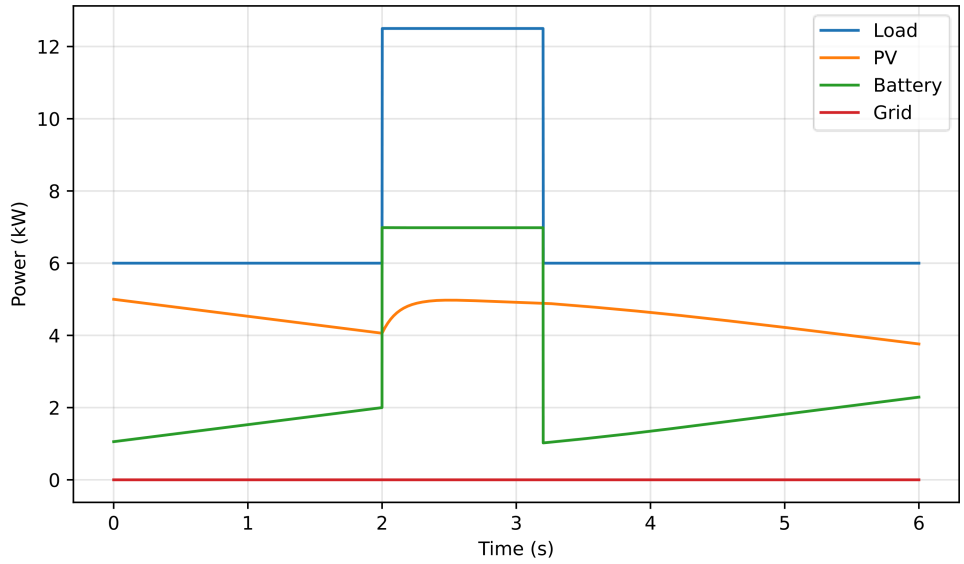


Figure 15. The dynamic power-sharing response during the islanded overload scenario (S12), showing the available PV and battery contribution, supplied load, and resulting unserved power after grid disconnection.

Following islanding, grid active-power exchange is forced to zero. During the overload interval, the available local generation and inverter capability are insufficient to satisfy the complete load demand. Consequently, part of the requested load remains unserved.

The peak unserved power reaches approximately 1.45 kW, while the accumulated unserved energy over the short overload interval is approximately 0.278 Wh. These quantities provide a direct measure of the practical backup limitation and are more informative for this scenario than conversion efficiency alone.

The corresponding DC-link voltage response is shown in Figure 16.

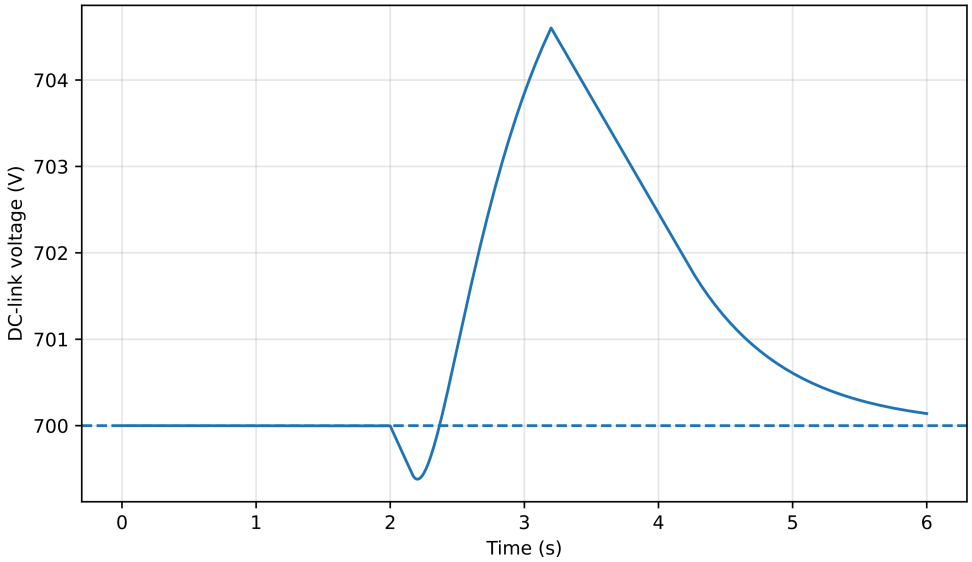


Figure 16. DC-link voltage response during the islanded overload scenario (S12). The dashed blue line represents the reference DC-link voltage (700 V), while the solid blue line shows the actual DC-link voltage response.

The maximum absolute relative DC-link deviation is approximately 0.66%. Thus, although the inverter is unable to supply the complete load during the overload interval, the DC-link itself remains comparatively well regulated. The principal limitation is therefore associated with available power and inverter current capability rather than DC-link instability.

The RMS inverter current response is presented in Figure 17.

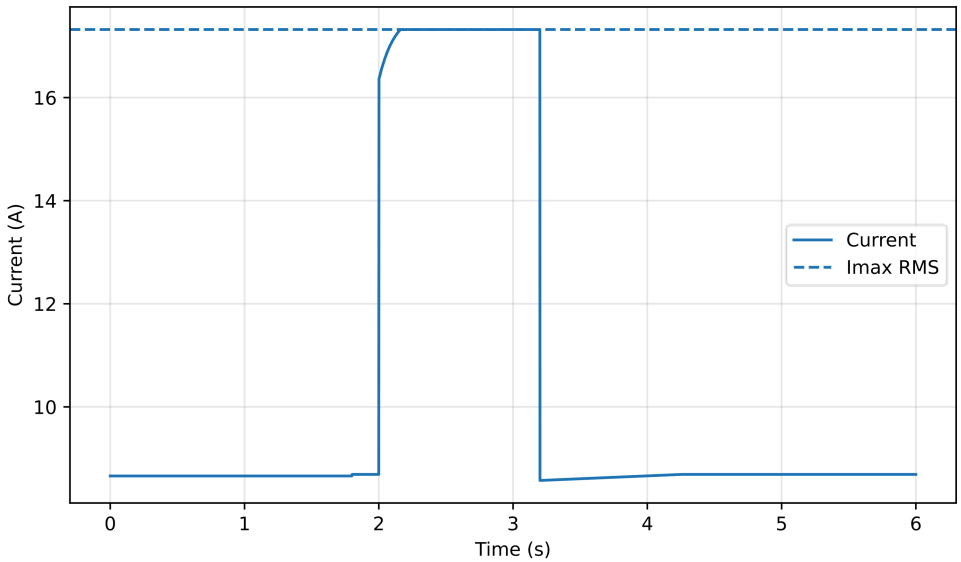


Figure 17. RMS inverter current during the islanded overload scenario (S12), showing sustained operation at the imposed current boundary.

The inverter current reaches approximately 17.32 A, corresponding to the imposed maximum RMS current. The current-limiting mechanism is active for approximately 20.0% of the complete 6 s simulation interval, which is the longest current saturation duration among the investigated scenarios.

The comparative harmonic stress indicators also increase during the overloaded islanded interval, reaching approximately $H_I \approx 8.80$ and $H_V \approx 3.30$.

As in the preceding scenarios, these values are dimensionless relative stress indicators and should not be interpreted as THD percentages.

The resulting HISI value is approximately 0.283. Although this value is lower than those obtained for the severe grid voltage sag and the transient export cases S4 and S8, the physical significance of S12 remains distinct. In this case, the limitation directly affects supply continuity: part of the requested load cannot be served even though the DC-link voltage remains stable.

Scenario S12 therefore demonstrates that nominal inverter power alone does not define practical backup capability. Islanded supply performance depends simultaneously on available PV generation, battery discharge capability, reactive-power demand, inverter apparent-power capacity, and the imposed current limit. For backup applications, peak unserved power and unserved energy are consequently essential performance indicators in addition to conventional electrical quantities.

3.7. Cross-Scenario Comparison Using HISI

To provide a unified comparison of the twelve investigated operating conditions, the calculated HISI values are summarized in Figure 18. As defined in Section 2.14, HISI combines normalized contributions associated with conversion efficiency penalty, DC-link voltage deviation, comparative harmonic stress, transient power imbalance, unintended grid export, current saturation, and unserved energy.

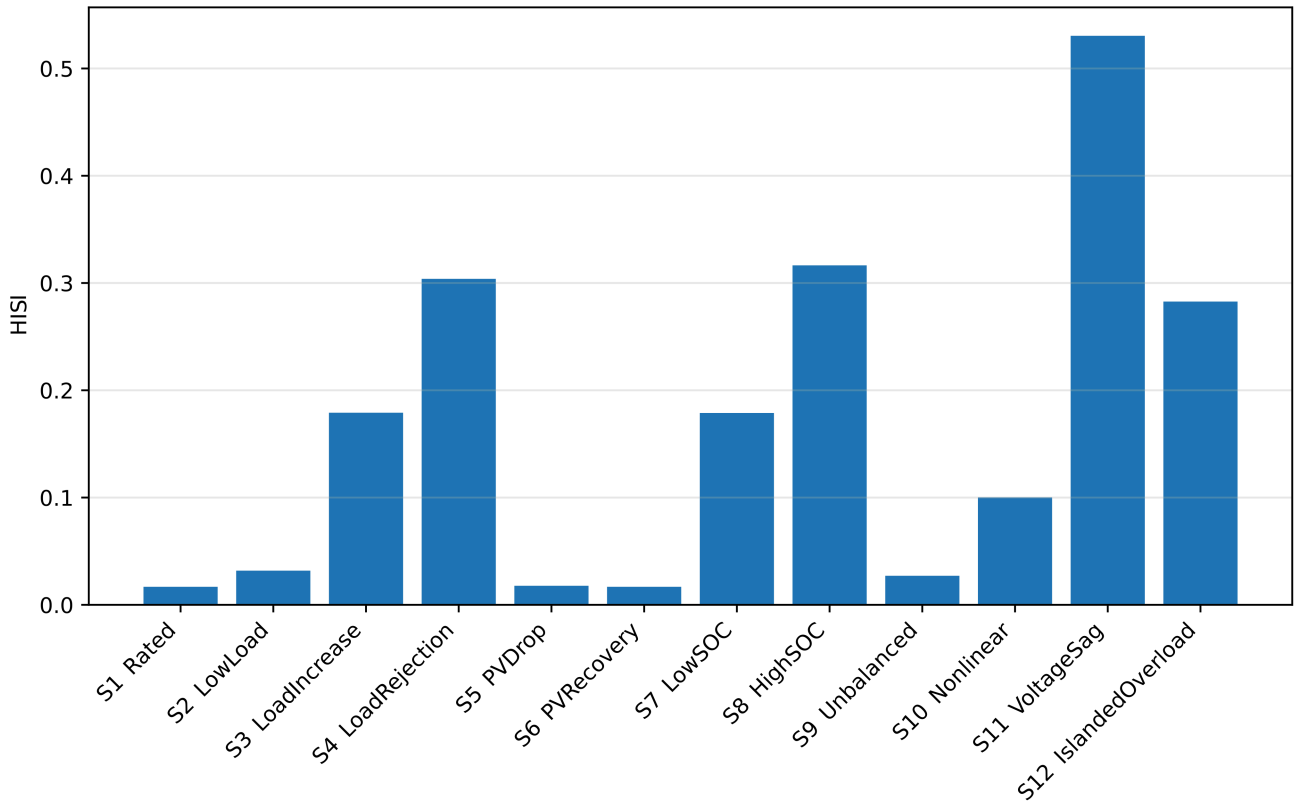


Figure 18. Hybrid Inverter Stress Index (HISI) for twelve investigated hybrid PV–battery inverter operating scenarios.

The calculated HISI values vary substantially across the investigated cases. The rated reference scenario (S1) and the rapid PV recovery scenario (S6) exhibit the lowest values, approximately 0.017, indicating operation with only minor normalized stress contributions. Similarly, S2, S5, and S9 remain comparatively low, with HISI values below approximately 0.04.

Intermediate values are obtained for S10, S7, and S3. The nonlinear load scenario (S10) reaches approximately 0.100, primarily because of the increased comparative harmonic stress contribution. The low-SOC scenario (S7) and the sudden load increase scenario (S3) produce HISI values of approximately 0.179, reflecting reduced battery operating margin and transient power imbalance, respectively.

Higher composite stress is observed for the three scenarios associated with substantial transient or constrained operation. The sudden load rejection case (S4) reaches a HISI value of approximately 0.304, while the high-SOC case (S8) reaches approximately 0.317. In both scenarios, the dominant contribution is associated with transient surplus power handling and unintended export rather than current saturation.

The islanded overload scenario (S12) produces a HISI value of approximately 0.283. Although this value is lower than those of S4 and S8, its physical interpretation is different because the dominant limitation is loss of supply capability, evidenced by sustained current saturation and non-zero unserved energy.

The highest HISI value is obtained for the severe grid voltage sag scenario (S11), approximately 0.530. This scenario simultaneously activates several stress mechanisms, including current saturation, reactive-current prioritization, DC-link deviation, transient power imbalance, and elevated comparative harmonic stress. The composite index therefore reflects the simultaneous reduction in operating margin across multiple domains.

The cross-scenario comparison confirms that similar HISI magnitudes can arise from fundamentally different physical mechanisms. For this reason, the HISI is not used as a substitute for the individual electrical indicators. Instead, it provides a compact comparative measure that complements the detailed interpretation of current saturation, unintended export, DC-link deviation, harmonic-related stress, and unserved load.

3.8. Quantitative Cross-Scenario Assessment

A quantitative comparison of the twelve investigated operating scenarios is presented in Table 4. The purpose of this comparison is to identify which physical limitations become dominant under different operating conditions and to demonstrate why inverter performance cannot be characterized using conversion efficiency alone.

Table 4. Quantitative performance indicators of the hybrid PV–battery inverter under the twelve investigated operating scenarios.

Scenario	Mean Efficiency (%)	Peak Export (kW)	Max. DC-Link Deviation (%)	H_I	Current Saturation (%)	Unserved Energy (Wh)	HISI
S1 Rated	98.50	0.000	0.000	1.800	0.00	0.000	0.017
S2 Low Load	96.23	0.000	0.000	2.280	0.00	0.000	0.032
S3 Load Increase	98.45	0.000	0.130	1.800	0.00	0.000	0.179
S4 Load Rejection	97.48	3.500	0.095	2.100	0.00	0.000	0.304
S5 PV Drop	98.50	0.000	0.001	1.800	0.00	0.000	0.018
S6 PV Recovery	98.50	0.000	0.000	1.800	0.00	0.000	0.017
S7 Low SOC	98.39	0.000	0.116	1.800	0.00	0.000	0.179
S8 High SOC	97.94	3.937	0.107	1.800	0.00	0.000	0.316
S9 Unbalanced Load	98.50	0.000	0.000	2.900	0.00	0.000	0.027
S10 Nonlinear Load	98.50	0.000	0.000	10.725	0.00	0.000	0.100
S11 Voltage Sag	98.50	2.281	4.662	14.300	10.83	0.000	0.530
S12 Islanded Overload	98.50	0.000	0.658	8.800	20.00	0.278	0.283

The values in Table 4 demonstrate that mean conversion efficiency alone provides little information about the dominant operating limitation. Several scenarios retain efficiencies close to 98.5% while exhibiting substantially different electrical behaviour. In particular, S11 and S12 maintain high mean efficiency despite activation of the inverter current limit, while S10 also remains near peak efficiency despite a substantial increase in the comparative harmonic stress indicator.

The load rejection scenario (S4) and high-SOC scenario (S8) exhibit a different type of limitation. Their peak unintended exports reach approximately 3.50 kW and 3.94 kW, respectively, without activation of the inverter current limit. Their maximum DC-link deviations remain below approximately 0.11%, indicating that the principal limitation is transient surplus power management rather than voltage instability or semiconductor current capability.

The comparison between S4 and S8 is particularly informative. Both scenarios involve temporary surplus generation, but S8 produces the larger reverse power excursion because the battery operates close to its upper SOC boundary. The reduced charging headroom therefore decreases the system's ability to absorb the sudden surplus before the PV curtailment mechanism responds.

Scenario S7 illustrates the opposite battery-related limitation. The final SOC reaches the imposed lower boundary of 20%, while the peak battery current reaches the maximum discharge limit of 17.5 A. Nevertheless, no inverter current saturation or unserved load occurs. Thus, the limitation originates within the battery subsystem rather than at the AC-side converter current boundary.

The nonlinear load scenario (S10) produces a maximum current-related harmonic stress indicator of approximately 10.73, while the unbalanced load scenario (S9) reaches approximately 2.90. Neither scenario activates the inverter current limiter or produces significant DC-link deviation. These cases therefore illustrate load-related electrical stress that is not visible from conventional active-power or efficiency indicators.

The voltage-sag scenario (S11) represents the strongest multi-domain disturbance. The maximum DC-link deviation reaches approximately 4.66%, the RMS inverter current reaches the imposed 17.32 A boundary, and the current limiter remains active for approximately 10.83% of the simulation interval. The current-related harmonic stress indicator also reaches its maximum value of approximately 14.30. The corresponding HISI value of approximately 0.530 reflects the simultaneous contribution of several different stress mechanisms.

The islanded overload case (S12) is distinguished by the loss of load supply capability. The inverter operates at its current limit for approximately 20% of the simulation interval and produces approximately 0.278 Wh of unserved energy, with a peak unserved power of approximately 1.45 kW. Thus, the principal consequence in this scenario is not grid interaction but insufficient local supply capability.

Overall, Table 4 confirms that the twelve scenarios expose different classes of operating constraints: transient export limitation, battery charge/discharge headroom, harmonic-related electrical stress, grid voltage-induced current saturation, and islanded supply deficiency. The HISI provides a compact supplementary measure of these effects, while the individual physical indicators remain necessary for identifying the actual cause of each limitation.

3.9. Identification of the Main Hidden Performance Limitations

The multi-scenario analysis reveals that the practical operating boundaries of the hybrid PV–battery inverter arise from several distinct physical mechanisms. These limitations cannot be reduced to a single rated-power or efficiency constraint because different scenarios activate different parts of the system model.

The first limitation is associated with transient surplus power management and zero-export capability. Scenarios S4 and S8 demonstrate that substantial short-duration reverse power flow can occur even when the supervisory controller is configured to minimize export. In S4, the abrupt reduction in local demand produces a peak unintended export of approximately 3.50 kW, whereas S8 reaches approximately 3.94 kW because the battery operates close to its upper SOC boundary. The comparison shows that zero-export performance depends not only on controller response speed but also on the instantaneous charging headroom available in the battery.

The second limitation concerns battery operating headroom. Scenarios S7 and S8 show that the same nominal storage capacity can provide markedly different short-term flexibility depending on the battery state. Near the lower SOC limit, discharge capability becomes constrained by the electrical and SOC boundaries of the battery model. Near the upper SOC limit, reduced charging headroom limits the ability of the battery to absorb a sudden surplus. Battery SOC should therefore be interpreted not only as an energy state variable, but also as an operational reserve influencing the dynamic flexibility of the hybrid inverter.

The third limitation is related to load-dependent electrical stress. Scenario S10 produces a pronounced increase in the current-related comparative harmonic stress indicator, reaching approximately H_I = 10.73, while the inverter remains below its RMS current limit and the DC-link voltage remains well controlled. Scenario S9 similarly introduces additional unbalance-related stress without activating the principal power or current constraints.

These cases demonstrate that acceptable active-power balance and conversion efficiency do not necessarily imply low electrical waveform-related stress.

The fourth limitation is associated with current-limited operation during grid voltage disturbances. Scenario S11 demonstrates that a severe voltage sag simultaneously increases current demand and activates LVRT-oriented reactive-current support. Because active and reactive current share the same finite converter current circle, increased reactive-current demand reduces the remaining active-current capability. The inverter reaches its maximum RMS current of approximately 17.32 A, and current saturation remains active for approximately 10.83% of the simulation interval. The accompanying DC-link deviation and power imbalance confirm that the disturbance affects both the AC-side current allocation and the DC-side energy balance.

The fifth limitation concerns islanded supply capability. Scenario S12 shows that once utility grid support is removed, the load that can be maintained is determined jointly by the instantaneous PV power, battery discharge capability, inverter apparent-power rating, reactive demand, and current limit. During the overload interval, the inverter remains at its current boundary for approximately 20% of the simulation interval and part of the requested load cannot be supplied. The peak unserved power is approximately 1.45 kW, corresponding to approximately 0.278 Wh of unserved energy over the short disturbance interval.

Taken together, these results show that the operating envelope of a hybrid PV–battery inverter is fundamentally multi-dimensional. Rated active power and peak conversion efficiency describe only a limited part of the achievable performance. Transient export capability, battery SOC headroom, comparative harmonic stress, current circle limitation, DC-link response, and islanded supply deficiency must also be considered when assessing the practical operating boundaries of the system.

3.10. Implications for Hybrid Inverter Specification and Control

The results have several practical implications for the specification, control, and assessment of hybrid PV–battery inverters.

First, zero-export capability should be characterized dynamically rather than solely through steady-state measurements. Scenarios S4 and S8 demonstrate that a controller may restore the desired operating condition after a disturbance while still allowing for substantial short-duration reverse power excursion. For this reason, peak unintended export, exported transient energy, and export violation duration provide more informative measures of zero-export performance than a single steady-state grid power value.

Second, the battery SOC operating window should be treated as part of the available control reserve. Operation close to the upper SOC boundary reduces the short-term ability of the storage system to absorb sudden PV surpluses, whereas operation close to the lower SOC boundary restricts additional discharge capability. Therefore, energy management strategies intended to maximize stored energy should also account for the dynamic flexibility required to manage fast load and generation changes.

Third, backup capability should not be specified only by nominal inverter active power. Scenario S12 shows that practical islanded supply capability depends simultaneously on PV availability, battery discharge limits, inverter apparent-power rating, reactive-power demand, and maximum current. Peak unserved power and unserved energy are therefore useful complementary quantities when evaluating backup operation.

Fourth, grid support performance during voltage sags is fundamentally constrained by the inverter current circle. In S11, LVRT-oriented reactive-current support competes directly with active-current transfer within the fixed current capability of the converter. Consequently, a controller that prioritizes reactive support may reduce the available active-

power margin even when sufficient DC-side energy remains available. Current-limiting behaviour should therefore be considered explicitly when specifying or comparing inverter grid support functions.

Fifth, conversion efficiency and RMS current are insufficient indicators of electrical stress under non-ideal load conditions. Scenario S10 demonstrates that the comparative harmonic stress indicators can increase substantially while the inverter remains within its RMS current and DC-link limits. Load-related electrical stress should therefore be assessed separately from conventional power transfer and efficiency metrics.

Finally, the results support the use of a multi-indicator assessment framework rather than reliance on a single aggregate metric. The HISI provides a compact secondary measure for cross-scenario comparison, but its interpretation should remain linked to the underlying physical quantities. For engineering assessment, the individual indicators, such as unintended export, DC-link deviation, current saturation, harmonic-related stress, and unserved energy remain essential for identifying the actual limitation mechanism and selecting an appropriate mitigation strategy.

Overall, the proposed framework can support early-stage inverter specification by identifying which subsystem or control constraint is most likely to become dominant under a given operating condition. This type of screening can help prioritize subsequent switching-level simulation, hardware-in-the-loop testing, or experimental validation toward the scenarios that impose the most significant operational stress.

4. Discussion and Limitations of the Study

The results demonstrate that the practical operating envelope of a hybrid PV–battery inverter is determined by the interaction of several constraints rather than by rated active power or peak conversion efficiency alone. Across the investigated scenarios, the mean conversion efficiency remains comparatively high in many cases, while the dominant limitation shifts between transient surplus power management, battery operating headroom, inverter current capability, load-related electrical stress, and islanded supply deficiency. The multi-scenario approach therefore provides information that is not available from conventional steady-state inverter specifications.

A particularly important result concerns the dynamic interpretation of zero-export operation. The revised simulations show that substantial instantaneous reverse power excursions may occur even when the supervisory controller ultimately restores the desired operating condition. Following sudden load rejection, the peak unintended export reaches approximately 3.50 kW, whereas operation close to the upper battery SOC boundary increases the corresponding peak to approximately 3.94 kW. The associated exported energies remain small, indicating that these events are transient, but their peak magnitude may still be relevant in installations where reverse power flow is tightly restricted. The comparison also demonstrates that zero-export capability depends not only on controller bandwidth but on the instantaneous charging reserve of the battery.

The revised battery representation provides a more physically meaningful basis for interpreting this effect than an energy-only SOC model. The first-order Thevenin equivalent circuit explicitly incorporates SOC-dependent open-circuit voltage, ohmic voltage drop, polarization dynamics, current limits, terminal voltage constraints, and charge/discharge power boundaries. Consequently, the reduced flexibility observed near the SOC limits emerges from explicit electrical and state constraints rather than from an imposed linear derating function. This is particularly relevant to S7 and S8, which expose the asymmetric consequences of operation close to the lower and upper SOC boundaries.

The voltage-sag scenario reveals a fundamentally different limitation. When the grid voltage is reduced to 0.55 pu, the LVRT-oriented controller introduces additional

reactive-current demand while the inverter simultaneously attempts to maintain active-power transfer. Because the active- and reactive-current components share the same finite current circle, the converter reaches its imposed RMS current limit of approximately 17.32 A. Current saturation remains active for approximately 10.83% of the simulation interval, while the maximum DC-link deviation increases to approximately 4.66%. This behaviour illustrates the direct coupling between AC-side current allocation and DC-side energy balance during severe grid disturbance.

The islanded overload case exposes another form of operating boundary. In grid-connected mode, temporary power deficits can be compensated by utility import. After islanding, however, the achievable local supply becomes entirely dependent on instantaneous PV generation, battery discharge capability, converter apparent-power rating, reactive-power demand, and inverter current limit. In S12, the inverter remains at its current boundary for approximately 20% of the simulation interval, while the peak unserved power reaches approximately 1.45 kW and the accumulated unserved energy reaches approximately 0.278 Wh. These results show why nominal inverter power alone is insufficient to characterize practical backup capability.

The nonlinear load scenario further demonstrates the need for multi-domain assessment. The inverter remains below its RMS current limit and the DC-link remains well controlled, yet the current-related comparative harmonic stress indicator increases substantially relative to the rated reference case. This response is not interpreted as a formal THD prediction. Instead, it provides a relative measure of the additional electrical stress associated with the prescribed nonlinear load condition. The result illustrates that acceptable active-power balance, conversion efficiency, and RMS current do not necessarily imply low waveform-related electrical stress.

The Hybrid Inverter Stress Index (HISI) provides a compact way to aggregate these different effects, but its role must be interpreted carefully. The index does not represent physical ageing, remaining lifetime, probability of failure, or a regulatory compliance score. Its numerical value depends on the selected normalization constants and weighting coefficients. Accordingly, the HISI is used only as a secondary comparative indicator, while the individual physical quantities remain the primary basis for identifying the actual limitation mechanism. The $\pm 30\%$ weighting-factor sensitivity analysis introduced in Section 2.14 is intended to evaluate how strongly the composite values depend on the adopted weighting assumptions.

Several limitations of the present study should be recognized.

First, the inverter is represented by an averaged dq-frame model rather than a switching-level electromagnetic model. This enables efficient evaluation of multiple operating scenarios but does not reproduce individual PWM switching events, carrier-frequency effects, dead time, semiconductor commutation transients, or device-specific switching losses. The present results should therefore be interpreted as system-level dynamic behaviour rather than detailed waveform predictions.

Second, the comparative harmonic stress indicators H_I and H_V are phenomenological screening quantities. They are designed to reflect the relative influence of nonlinear loading, unbalance, voltage sag, low loading, and current saturation within the investigated framework. Because the model does not generate complete phase-domain switching waveforms, these indicators cannot be interpreted as measured or simulated THD and cannot be used directly to demonstrate compliance with harmonic standards. Switching-level or experimental waveform analysis would be required for that purpose. This limitation is already explicitly reflected in the methodology.

Third, although the revised first-order Thevenin battery model captures short-term voltage, current, polarization, and SOC effects, it does not include detailed electrochemical

diffusion, temperature dependence, cell-to-cell imbalance, ageing, capacity fade, or state-of-health evolution. The battery representation is therefore appropriate for the second-scale dynamic assessment considered here but should not be interpreted as a long-term degradation model.

Fourth, the 6 s simulation horizon is intentionally limited to fast electrical and supervisory control phenomena. It cannot capture multi-hour or daily SOC drift, repeated cycling, seasonal PV variability, long-term load evolution, forecast uncertainty, or energy management optimization over extended horizons. Consequently, the present scenarios characterize short-term operating boundaries rather than the probability with which these conditions would occur during annual operation.

Fifth, the control structure is generic and is not intended to reproduce the proprietary firmware, battery management logic, anti-islanding implementation, LVRT response, or current priority strategy of a specific commercial inverter. Commercial products may therefore exhibit quantitatively different transient responses even when subjected to similar external disturbances. The numerical results should be interpreted as properties of the investigated model and control architecture rather than as performance claims for a particular manufacturer.

Sixth, the unbalanced and nonlinear load scenarios are represented at a reduced system level. The framework is suitable for comparative stress screening, but a detailed phase-domain negative-sequence model would be required to reproduce all electromagnetic consequences of asymmetric loading, and a switching or waveform-level model would be required for detailed nonlinear load spectral analysis.

Finally, the current study does not include laboratory, hardware-in-the-loop, or power-hardware-in-the-loop validation. Such validation would be especially valuable for the transient zero-export response, battery operation close to SOC boundaries, voltage-sag current limitation, islanded overload, and the calibration of the comparative harmonic stress indicators.

Despite these limitations, the framework provides a computationally efficient method for identifying operating conditions that deserve more detailed investigation. Its primary value lies in separating different limitation mechanisms within a common model and showing that acceptable performance in one domain does not guarantee sufficient operating margin in another. The framework can therefore serve as a pre-design and specification support tool prior to higher-fidelity switching simulations or experimental validation.

Future work should focus on switching-level validation of the most critical scenarios, phase-domain modelling of unbalanced operation, hardware-in-the-loop or experimental verification, electrothermal and ageing-aware extensions of the battery and converter models, longer-duration energy management studies, and application-specific calibration of the HISI normalization constants and weighting coefficients.

5. Conclusions

This study investigated the short-term performance boundaries of a hybrid PV–battery inverter under twelve operating scenarios extending beyond conventional rated-power and peak efficiency characterization. The results demonstrate that satisfactory conversion efficiency alone does not guarantee adequate dynamic, grid support, power quality-related, or backup performance. Different operating conditions activate fundamentally different constraints within the PV source, battery, DC link, inverter current control system, and supervisory energy management layer.

The transient zero-export scenarios showed that reverse power excursions can occur even when the supervisory controller ultimately restores the intended operating condition. Following sudden load rejection, the peak unintended grid export reached approximately

3.50 kW, while operation close to the upper battery SOC boundary increased the peak export to approximately 3.94 kW. The comparison demonstrates that battery charging headroom is an important component of the dynamic flexibility available for suppressing short-duration surplus power.

The revised first-order Thevenin battery representation also showed that battery SOC should be interpreted not only as an energy state variable but also as an operating constraint. Near the lower SOC boundary, additional discharge capability becomes restricted, whereas operation close to the upper SOC boundary reduces the capability of the storage system to absorb a sudden power surplus. These effects arise from the combined SOC, current, terminal voltage, and battery power limits rather than from an imposed SOC-dependent derating function.

The severe grid voltage sag produced the strongest simultaneous activation of several inverter constraints. The RMS inverter current reached the imposed limit of approximately 17.32 A, current saturation was active for approximately 10.83% of the simulation interval, and the maximum DC-link deviation reached approximately 4.66%. The corresponding current- and voltage-related comparative harmonic stress indicators increased to approximately H_I = 14.30 and H_V = 5.80, respectively. These quantities are used only as dimensionless comparative indicators and should not be interpreted as standard-compliant THD values.

Under islanded overload operation, the inverter current remained at its imposed limit for approximately 20% of the investigated interval. The peak unserved power reached approximately 1.45 kW, corresponding to approximately 0.278 Wh of unserved energy. This result demonstrates that practical backup capability is governed jointly by instantaneous PV availability, battery discharge capability, inverter apparent-power rating, reactive demand, and current limitation rather than by nominal active power alone.

The proposed HISI provides a supplementary normalized comparison across scenarios governed by different physical mechanisms. The largest HISI value was obtained for the severe grid voltage sag, approximately 0.530, while the high-SOC, sudden load rejection, and islanded overload cases reached approximately 0.316, 0.304, and 0.283, respectively. The HISI is not intended as a lifetime, reliability, or compliance indicator; its role is to complement, rather than replace, the individual electrical and operational metrics.

Overall, this study confirms that the practical operating envelope of a hybrid PV–battery inverter is inherently multi-dimensional. Dynamic surplus power handling, battery operating headroom, DC-link regulation, finite current capability, comparative harmonic-related stress, and islanded supply capability should be considered together when evaluating inverter performance. The proposed multi-scenario framework provides a computationally efficient pre-design and specification support methodology for identifying which subsystem or control constraint becomes dominant under a given operating condition.

Future work should include switching-level and phase-domain validation of the critical scenarios, hardware-in-the-loop and experimental verification, electrothermal and ageing-aware battery and converter models, longer-duration energy management studies, and application-specific calibration of the HISI normalization constants and weighting coefficients.

Additional supporting results, including the normalized cross-scenario severity map (Figure S1), detailed scenario performance indicators (Table S1), HISI sensitivity analysis (Table S2), complete simulation datasets (Data S1 and Data S2), and the Python simulation code (Code S1), are provided in the Supplementary Materials.

Supplementary Materials: The following supporting information can be downloaded at https://www.mdpi.com/article/10.3390/en19204887/s1: Figure S1: Normalized cross-scenario severity map; Table S1: Detailed performance indicators for Scenarios S1–S12; Table S2: HISI sensitivity analysis under ±30% variations in the weighting coefficients; Data S1: Complete time-series datasets for all investigated scenarios; Data S2: Scenario-level summary results and HISI sensitivity analysis data; Code S1: Python source code for the final hybrid PV–battery inverter simulation model. The indicators HI and HV represent dimensionless comparative harmonic stress measures and should not be interpreted as total harmonic distortion (THD) values.

Author Contributions: Conceptualization, P.S. and N.H.; methodology, P.S.; software, P.S.; validation, P.S. and N.H.; formal analysis, P.S.; investigation, P.S.; resources, N.H.; data curation, P.S.; writing—original draft preparation, P.S.; writing—review and editing, P.S. and N.H.; visualization, P.S.; supervision, N.H. and P.S.; project administration, P.S. and N.H. All authors have read and agreed to the published version of the manuscript.

Funding: This research was supported by the European Union through the Recovery and Resilience Facility under the Bulgarian National Recovery and Resilience Plan, within the procedure "Establishing a Network of Research Higher Education Institutions in Bulgaria", Project No. BG-RRP-2.004-0005, "Improving the Research Capacity and Quality to Achieve International Recognition and Resilience of TU-Sofia (IDEAS)". The equipment used in this study was funded by the European Union through the European Regional Development Fund (ERDF) under the Programme "Research, Innovation and Digitalisation for Smart Transformation" 2021–2027, Project No. BG16RFPR002-1.014-0006, "National Centre of Excellence Mechatronics and Clean Technologies".

Data Availability Statement: The data supporting the findings of this study are available within the article and the accompanying Supplementary Materials submitted with the manuscript.

Acknowledgments: The authors gratefully acknowledge the support of the European Regional Development Fund under the Programme "Research, Innovation and Digitalisation for Smart Transformation" 2021–2027. The research equipment used in this study was funded within Project BG16RFPR002-1.014-0006, "National Centre of Excellence Mechatronics and Clean Technologies". The availability of this research infrastructure contributed to the successful experimental implementation of the present work.

Conflicts of Interest: The authors declare no conflicts of interest.

Abbreviations

AC	Alternating Current
BESS	Battery Energy Storage System
CSV	Comma-Separated Value
DC	Direct Current
ECM	Equivalent Circuit Model
EMS	Energy Management System
H_I	Current-Related Harmonic Stress Indicator
H_V	Voltage-Related Harmonic Stress Indicator
HISI	Hybrid Inverter Stress Index
LFP	Lithium Iron Phosphate
LVRT	Low-Voltage Ride-Through
MPPT	Maximum Power-Point Tracking
PV	Photovoltaic
PWM	Pulse-Width Modulation
RMS	Root Mean Square
SOC	State of Charge
THD	Total Harmonic Distortion

References

1. Boscaino, V.; Ditta, V.; Marsala, G.; Panzavecchia, N.; Tinè, G.; Cosentino, V.; Cataliotti, A.; Di Cara, D. Grid-connected photovoltaic inverters: Grid codes, topologies and control techniques. *Renew. Sustain. Energy Rev.* **2023**, *189*, 113903. [CrossRef]
2. Meraj, S.T.; Yu, S.S.; Rahman, M.; Hasan, K.; Lipu, H.; Trinh, H. Energy management schemes, challenges and impacts of emerging inverter technology for renewable energy integration towards grid decarbonization. *J. Clean. Prod.* **2023**, *405*, 137002. [CrossRef]
3. Basnet, S.; Deschinkel, K.; Moyne, L.L.; Péra, M.C. A review on recent standalone and grid integrated hybrid renewable energy systems: System optimization and energy management strategies. *Renew. Energy Focus* **2023**, *46*, 103–125. [CrossRef]
4. Li, B.; Liu, Z.; Wu, Y.; Wang, P.; Liu, R.; Zhang, L. Review on photovoltaic with battery energy storage system for power supply to buildings: Challenges and opportunities. *J. Energy Storage* **2023**, *61*, 106763. [CrossRef]
5. Maka, A.O.M.; Chaudhary, T.N. Performance investigation of solar photovoltaic systems integrated with battery energy storage. *J. Energy Storage* **2024**, *84*, 110784. [CrossRef]
6. Benavides, D.; Arévalo, P.; Criollo, A.; Tostado-Véliz, M.; Jurado, F. Multi-mode monitoring and energy management for photovoltaic-storage systems. *Renew. Energy* **2024**, *230*, 120820. [CrossRef]
7. Balogun, O.A.; Sun, Y.; Gbadega, P.A. Coordination of smart inverter-enabled distributed energy resources for optimal PV-BESS integration and voltage stability in modern power distribution networks: A systematic review and bibliometric analysis. *e-Prime-Adv. Electr. Eng. Electron. Energy* **2024**, *10*, 100800. [CrossRef]
8. Dagal, I. Real time adaptive control of photovoltaic battery systems: Integrated management of state of charge, voltage regulation, and irradiance fluctuations. *J. Energy Storage* **2026**, *152*, 120765. [CrossRef]
9. Ali Khan, M.Y.; Liu, H.; Yang, Z.; Yuan, X. A Comprehensive Review on Grid Connected Photovoltaic Inverters, Their Modulation Techniques, and Control Strategies. *Energies* **2020**, *13*, 4185. [CrossRef]
10. Talha, M.; Amir, A.; Raihan, S.R.S.; Rahim, N.A. Grid-connected photovoltaic inverters with low-voltage ride through for a residential-scale system: A review. *Int. Trans. Electr. Energy Syst.* **2020**, *31*, e12630. [CrossRef]
11. Kumar, P.; Malik, N.; Garg, A. Comparative analysis of solar—Battery storage sizing in net metering and zero export systems. *Energy Sustain. Dev. Sustain. Dev.* **2022**, *69*, 41–50. [CrossRef]
12. Sharma, V.; Haque, M.H.; Aziz, S.M.; Kauschke, T. Smart inverter and battery storage controls to reduce financial loss due to overvoltage-induced PV curtailment in distribution feeders. *Sustain. Energy Grids Netw.* **2023**, *34*, 101030. [CrossRef]
13. Yildiz, B.; Stringer, N.; Klymenko, T.; Samhan, M.S.; Abramowitz, G.; Bruce, A.; MacGill, I.; Egan, R.; Sproul, A.B. Real-world data analysis of distributed PV and battery energy storage system curtailment in low voltage networks. *Renew. Sustain. Energy Rev.* **2023**, *186*, 113696. [CrossRef]
14. González-Moreno, A.; Marcos, J.; De La Parra, I.; Marroyo, L. Control method to coordinate inverters and batteries for power ramp-rate control in large PV plants: Minimizing energy losses and battery charging stress. *J. Energy Storage* **2023**, *72*, 108621. [CrossRef]
15. Huseinbegović, S.; Smajkić, A.; Ahmethodžić, L.; Smaka, S.; Gajip, S. Optimal building integrated photovoltaic sizing approach according to load profile under zero export restrictions with real data validation. *Renew. Energy Focus* **2024**, *50*, 100605. [CrossRef]
16. Zhou, H.S.; Passey, R.; Bruce, A.; Sproul, A.B. Impact of residential battery energy storage systems on the peak reverse power flows from distributed photovoltaic systems. *J. Energy Storage* **2022**, *52*, 104817. [CrossRef]
17. Motamedisedeh, O.; Omrani, S.; Karim, A.; Drogemuller, R.; Walker, G. A comprehensive review of optimum integration of photovoltaic-based energy systems. *Renew. Sustain. Energy Rev.* **2024**, *207*, 114935. [CrossRef]
18. Alrbai, M.; Al-Ghussain, L.; Al-Dahidi, S.; Ayadi, O.; Al-Naser, S. Techno-economic assessment of residential PV system tariff policies in Jordan. *Util. Policy* **2025**, *93*, 101894. [CrossRef]
19. Jamroen, C.; Sirisukprasert, S. A voltage regulation strategy with state of charge management using battery energy storage optimized by a self-learning particle swarm optimization. *Comput. Electr. Eng.* **2022**, *101*, 108103. [CrossRef]
20. Shuvra, M.A.; Chowdhury, B. Reconfigurable and flexible voltage control strategy using smart PV inverters with integrated energy storage for advanced distribution systems. *IET Smart Grid* **2019**, *3*, 22–30. [CrossRef]
21. Zhang, Z.; Zuo, Z.; Wang, Y. Distributed control for state-of-charge balance and load voltage regulation in DC microgrids with clustered generations. *Asian J. Control* **2022**, *24*, 3456–3465. [CrossRef]
22. Dutta, A.; Ganguly, S.; Kumar, C. Coordinated control scheme for EV charging and volt/var devices scheduling to regulate voltages of active distribution networks. *Sustain. Energy Grids Netw.* **2022**, *31*, 100761. [CrossRef]
23. Baeckeland, N.; Chatterjee, D.; Lu, M.; Johnson, B.; Seo, G.S. Overcurrent Limiting in Grid-Forming Inverters: A Comprehensive Review and discussion. *IEEE Trans. Power Electron.* **2024**, *39*, 14493–14517. [CrossRef]
24. Ordono, A.; Sanchez-Ruiz, A.; Zubiaga, M.; Asensio, F.J.; Cortajarena, J.A. Current limiting strategies for grid forming inverters under low voltage ride through. *Renew. Sustain. Energy Rev.* **2024**, *202*, 114657. [CrossRef]
25. Qoria, T.; Wang, X.; Kadri, R. Grid-forming control VSC-based including current limitation and re-synchronization functions to deal with symmetrical and asymmetrical faults. *Electr. Power Syst. Res.* **2023**, *223*, 109647. [CrossRef]

26. Zhang, H.; Xiong, L.; Gao, Z.; Yu, S.; Zhang, X. Power matching based current limitation method for grid forming converter under large disturbances. *Int. J. Electr. Power Energy Syst.* **2024**, *157*, 109841. [CrossRef]
27. Kkuni, K.V.; Yang, G. Effects of current limit for grid forming converters on transient stability: Analysis and solution. *Int. J. Electr. Power Energy Syst.* **2024**, *158*, 109919. [CrossRef]
28. Desai, M.A.; He, X.; Huang, L.; Dörfler, F. Saturation-informed current-limiting control for grid-forming converters. *Electr. Power Syst. Res.* **2024**, *234*, 110746. [CrossRef]
29. Liemann, S.; Rehtanz, C. Voltage stability analysis of grid-forming converters with current limitation. *Electr. Power Syst. Res.* **2024**, *235*, 110820. [CrossRef]
30. Ávila-Martínez, R.E.; Renedo, J.; Rouco, L.; Garcia-Cerrada, A.; Sigrist, L.; Guillaud, X.; Qoria, T. Impact of current limiters and fast voltage boosters in grid-forming VSC-based generators on transient stability. *Electr. Power Syst. Res.* **2024**, *235*, 110753. [CrossRef]
31. Baeckeland, N.; Venkatramanan, D.; Kleemann, M.; Dhople, S. Stationary-Frame Grid-Forming inverter control architectures for unbalanced Fault-Current limiting. *IEEE Trans. Energy Convers.* **2022**, *37*, 2813–2825. [CrossRef]
32. Khan, I.; Doolla, S. Improved Fault Ride-Through response of grid forming inverters under symmetrical and asymmetrical faults. *IEEE Trans. Energy Convers.* **2024**, *40*, 394–408. [CrossRef]
33. Sekizaki, S.; Sasaki, Y.; Zoka, Y.; Yorino, N.; Higashi, K.; Miyamoto, K.; Yamada, T. Single-phase synchronous inverter control for fault management using emulation signal generators. *Electr. Power Syst. Res.* **2024**, *234*, 110681. [CrossRef]
34. Pal, A.; Achlerkar, P.D.; Panigrahi, B.K. Fault-induced current limitation control for grid-forming inverters: A framework for rapid grid code compliance. *Electr. Power Syst. Res.* **2025**, *242*, 111471. [CrossRef]
35. Fan, Y.; Han, M.; Wang, S.; Zhang, L.; Xie, W. Transient stability Analysis of Grid-Forming converter in current limiting Mode based on Hamiltonian Theory. *IEEE Trans. Power Deliv.* **2024**, *40*, 1836–1846. [CrossRef]
36. Chen, J.; Gong, Q.; Zhang, Y.; Fawad, M.; Wang, S.; Li, C.; Liang, J. Comprehensive assessment of transient stability for Grid-Forming Converters considering current limitations, inertia and damping effects. *CSEE J. Power Energy Syst.* **2025**, *11*, 1–12. [CrossRef]
37. Westman, J.; Hadidi, R. Overload mitigation for grid-forming inverters in islanded microgrids with synchronous generators. *Electr. Power Syst. Res.* **2024**, *239*, 111231. [CrossRef]
38. Ullah, M.; Guan, Y.; Barrios, M.A.; Vasquez, J.C.; Guerrero, J.M. Dynamic Response of Droop-Controlled Grid-Forming Inverters Under Varying Grid Impedances for Enhanced Stability in Microgrids. *Appl. Sci.* **2025**, *15*, 12562. [CrossRef]
39. Salagamsetty, L.; Cai, L. Power-Hardware-in-loop test of a Grid-Forming Converter. In Proceedings of the 6th Global Power, Energy and Communication Conference (GPECOM), Budapest, Hungary, 4 June 2024; pp. 832–837. [CrossRef]
40. *IEEE Std 1547-2018*; IEEE Standard for Interconnection and Interoperability of Distributed Energy Resources with Associated Electric Power Systems Interfaces. IEEE: New York, NY, USA, 2018. [CrossRef]
41. *BDS EN 50549-1:2019/A1:2024*; Requirements for Generating Plants to be Connected in Parallel with Distribution Networks—Part 1: Connection to a LV Distribution Network—Generating Plants up to and Including Type B. Bulgarian Institute for Standardization: Sofia, Bulgaria, 2024. Available online: https://bds-bg.org/en/project/show/bds:proj:119065 (accessed on 12 October 2026).

Disclaimer/Publisher's Note: The statements, opinions and data contained in all publications are solely those of the individual author(s) and contributor(s) and not of MDPI and/or the editor(s). MDPI and/or the editor(s) disclaim responsibility for any injury to people or property resulting from any ideas, methods, instructions or products referred to in the content.